CHALMERS

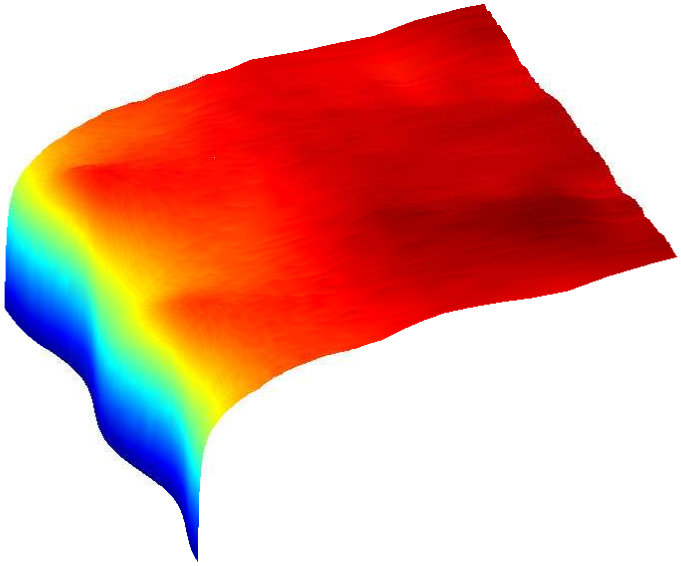

Large Eddy Simulation of Flow and Heat Transfer in a Pipe With Corrugated Walls

Daniel Lindroth

Department of Applied Mechanics
Division of Fluid Dynamics
Chalmers University of Technology
Göteborg Sweden, 2013

Master's Thesis [2013 : 13]

Master's Thesis 2013:13

Large Eddy Simulation of Flow and Heat Transfer in a Pipe With Corrugated Walls

Master's Thesis

Daniel Lindroth

Department of Applied Mechanics
Division of Fluid Dynamics
Chalmers University of Technology
Göteborg, Sweden, 2013

Large Eddy Simulation of Flow and Heat Transfer in a Pipe With Corrugated Walls

Master's Thesis

Daniel Lindroth

Master's Thesis 2013:13
ISSN: 1652-8557

Department of Applied Mechanics,
Division of Fluid Dynamics
Chalmers University of Technology
Se-412 96 Göteborg, Sweden
Phone +46-(0)31-7721400
Fax: +46-(0)31-180976

Printed at Chalmers Reproservice
Göteborg, Sweden 2013

Large Eddy Simulation of Flow and Heat Transfer in a Pipe With Corrugated Walls

Master's Thesis

by

Daniel Lindroth
daniel.lindroth@chalmers.se
Department of Applied Mechanics
Division of Fluid Dynamics
Chalmers University of Technology

Abstract

Large Eddy Simulation of the flow and heat transfer on the inside of a pipe with corrugated walls has been conducted on a fluid with Prandtl number $Pr = 3.5$, at Reynolds number $Re_d = 10^4$. The system's friction coefficient C_f, dimensionless pressure drop and Nusselt number Nu based on the simulation are presented and compared to a straight pipe. Some basic properties connected to the characteristics of the flow and thermal properties of the simulation are discussed. It is hypothised that the local loss in performance is related to the accumulation of the periodic wall temperature and that the increase in performance is related to the decreasing radius of the corrugated pipe.

Keywords: LES, heat transfer, corrugated pipe

Acknowledgement

I'd like to direct special thanks to my supervisor professor Lars Davidson for all his support, guidance and encouragement during my work on this thesis. His effort has been invaluable.

Further I'd like to thank Fredrik Innings at Tetra Pak for the opportunity to do this thesis.

I'd also like to thank Maryam Mirzaei for rewarding discussions in the beginning of the project.

Finally, thanks to my wonderful wife Hanna for all her support and to my daughter Nova for inspiration.

Nomenclature

Upper-case Roman

C_f	Friction coefficient
L	Periodic pipe length
m	Mass
Nu	Nusselt number
Nu_{str}	Nusselt number for a straight pipe
Pr	Prandtl number
$\mathscr{P}$	Periodic pressure
Q	Heat rate
R	Pipe radius
Re_ℓ	Reynolds number based on scale ℓ
Re_R	Reynolds number based on the pipe radius
Re_τ	Reynolds number based on wall friction
S	General source term
T	Temperature

Lower-case Roman

c_p	Specific heat
e	Internal energy
ℓ	Length scale
p	Global pressure field
q	Constant heat flux
t	Time parameter
v_r	Velocity in the radial direction
u	Velocity in the streamwise direction
u_b	Bulk velocity
u_i	Velocity component in direction i
u^+	Velocity wall coordinate
x_i	Spatial coordinate in direction i
y^+	Radial wall coordinate

Upper-case Greek

Δp^*	Dimensionless pressure drop
$\Delta x, \Delta y, \Delta z$	Streamwise, radial and spanwise mesh spacings

Γ	Generic function for material properties
Ω	Volume

Lower-case Greek

β	Pressure drop over the periodic length
δ_{ij}	Kroneckers delta symbol
η	Kolmogorov length scale
ν	Kinematic viscosity
ρ	Density
σ	Temperature difference over the periodic length
ϕ	Generic transported scalar quantity

Contents

Chapter 1

Introduction

This introduction gives a short background to the thesis followed by the purpose and goal. Three research questions are then introduced and the delimitations of the study are mentioned.

1.1 Background

Exchanging heat between fluids at different temperature through a separating solid wall is an important process used in many engineering applications such as space heating, air-conditioning, production of power or recovery of otherwise wasted heat to name a few. A more specific application is related to food processing where the need to effectively heat a fluid at a low energy cost, in terms of controlling the system, is of paramount importance.

One type of irreducible configuration of a heat exchanger is to arrange a counterparallel flow through concentric tubes. A schematic heat exchanger using counterparallel flows is shown in figure 1.1. If the flow velocities are large enough, the heat transfer mode of forced convection will dominate the energy transport from the hot to the cold fluid. The shape of the thermal boundary layer will then be a dominating factor in the efficiency of heat transfer to the cold fluid [1]. Changing the geometry of the pipes introduces modifications to the thermal boundary layer and opens the potential for a more efficient heat transfer between the fluids.

Tetra Pak is a major actor in the line of packaging and food processing technology. In their production there is machinery used for heat treatment of food products. Heat exchanger technology is an important part and it is in their interest to offer machinery of high quality concerning energy use and

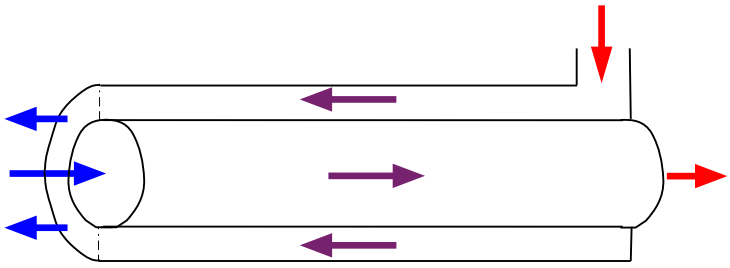

Figure 1.1: Schematic over heat exchanger with counterparallel flow

efficiency in the intended application.

The company is researching new possibilities to be used in the next generation of heat treatment in food processing. As a step in this research, there is an interest in a numerical investigation of the behavior of the heat transfer to the inside of a heat exchanger of the type shown in figure 1.1, with the addition of a corrugated geometry.

1.2 Purpose and goal

The purpose of the present study is to increase the knowledge regarding the behavior of heat transfer in a heat exchanger with a corrugated wall. The goal is to perform a numerical investigation of the heat transfer properties, using Computational Fluid Dynamics, on the inside of a heat exchanger with a specific corrugated geometry as depicted in figure 1.2, and compare the result with the performance of a straight tube heat exchanger.

1.3 Research questions

The present study aims at answering the questions:

1. What is the quantified heat transfer, expressed in a Nusselt number, between the separating wall and the interior of the corrugated heat exchanger?

2. How large is the friction coefficient, i.e. in the interior of the heat exchanger compared to a straight pipe?

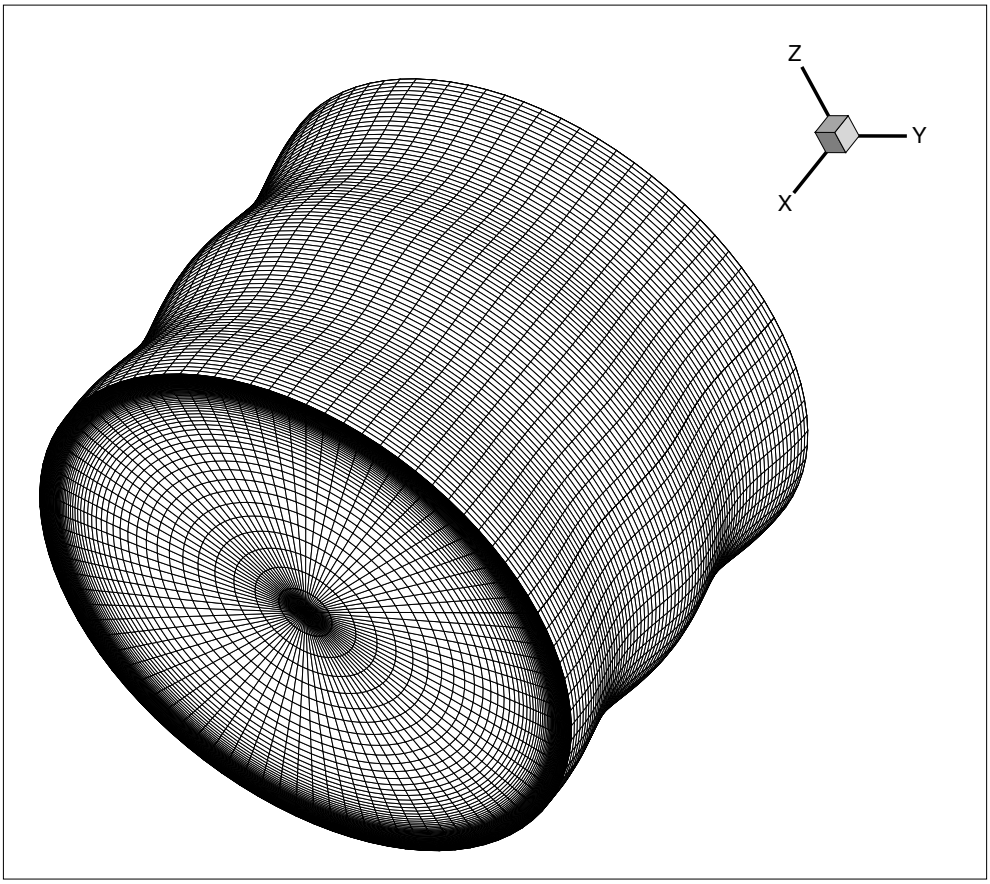

Figure 1.2: Computational mesh for the inner side of a two pitch section, corrugated heat exchanger

3. How does the geometry perform compared to a straight pipe geometry?

1.4 Delimitations

The present study is a numerical investigation and no experiments other than simulations are performed. Further the study is deliberately limited to a specific geometrical configuration only.

Chapter 2

Governing Equations

In the first section of this chapter the basic equations governing the flow and temperature are introduced. In the next section the concept of Large Eddy Simulations is introduced and modifications to the basic equations are discussed. Finally, in the last section, methods and modifications necessary for geometries with periodic variations are treated. This treatment is based on the article *Fully Developed Flow and Heat Transfer in Ducts Having Streamwise-Periodic Variations of Cross-Sectional Area* by Patankar et. al. [2].

2.1 Basic equations

Simulations of physical systems necessarily involves simplifications by introduction of idealised abstractions in the form of models that aim at predicting the behavior of the systems. When modeling fluids basic assumptions are made. Mass, momentum and energy are taken as conserved quantities and the continuum hypothesis is assumed to hold; it is assumed that molecular interactions in the fluid are of such large extent that fluctuations in the physical properties of the fluid evens out sufficiently to be described by continuous fields [3], [4].

From these assumptions, a set of equations modeling change in internal energy and motion of the fluid can be formulated [5]. Further assumptions about the nature of the fluid introduces the concept of incompressible fluids as fluids where pressure variations have no significant effect on the density. As a result the continuity equation for incompressible fluids, describing mass

conservation, takes a particularly simple form

$$\frac{\partial u_i}{\partial x_i} = 0, \tag{2.1.1}$$

where u_i is the velocity field and i is in the set $\{1, 2, 3\}$, repeated indices are summed according to Einsteins summation convention. Together with the assumption of constant viscosity, and neglecting all kinds of body forces, the momentum equations can be formulated as

$$\frac{\partial u_i}{\partial t} + \frac{\partial u_i u_j}{\partial x_j} = -\frac{1}{\rho}\frac{\partial p}{\partial x_j} + \nu\frac{\partial^2 u_i}{\partial x_j \partial x_j}, \tag{2.1.2}$$

where ρ is the density, p is the pressure and ν is the kinematic viscosity. This vector equation together with the continuity equation is called the Navier-Stokes equations, here presented in conservative form [5]. Assuming constant specific heat c_p the relation between the energy e and the temperature T is $e = c_p T$. The energy equation is then written as

$$\frac{\partial T}{\partial t} + \frac{\partial u_j T}{\partial x_j} = \frac{\nu}{Pr}\frac{\partial^2 T}{\partial x_j \partial x_j}, \tag{2.1.3}$$

where the Prandtl number $Pr = c_p \nu / \rho k$ is introduced, k being the thermal conductivity.

2.2 Large Eddy Simulations

In a turbulent flow the size of the smallest structures can be estimated, with the use of dimensional analysis, to be of the Kolmogorov length η

$$\frac{\eta}{\ell} \sim \mathrm{Re}_\ell^{-3/4}, \tag{2.2.1}$$

where ℓ is the largest length scale in the flow and Re_ℓ is the Reynolds number based on ℓ [6]. To solve a discretised version of equations (2.1.1), (2.1.2) and (2.1.3) it is then necessary to introduce a computational grid that is capable of resolving structures on the scale of η. If the Reynolds number is high, the computational cost is also high. There are methods to reduce the need of full resolution by introducing models of the turbulent behaviour on the smallest spatial scales.

One such method is the Large Eddy Simulation (abbreviated LES) method. Here a spatial filtering operation that smoothens the turbulent behavior by

removing the smallest spatial scales is introduced. After filtering, the resulting equations will contain a subgrid scale (abbreviated sgs) stress tensor. This stress tensor describes how the removed scales interacts with the resolved scales. The tensor is not known a priori, since it is dependent on the removed scales, so a model needs to be introduced for its behavior [7].

After filtering the system of equations (2.1.1), (2.1.2) and (2.1.3) it will take the form

$$\frac{\partial \bar{u}_i}{\partial x_i} = 0, \tag{2.2.2}$$

$$\frac{\partial \bar{u}_i}{\partial t} + \frac{\partial \bar{u}_i \bar{u}_j}{\partial x_j} = -\frac{1}{\rho}\frac{\partial \bar{p}}{\partial x_i} + \frac{\partial}{\partial x_j}\left[(\nu + \nu_t)\frac{\partial \bar{u}_i}{\partial x_j}\right], \tag{2.2.3}$$

$$\frac{\partial \bar{T}}{\partial t} + \frac{\partial \bar{u}_j \bar{T}}{\partial x_j} = \frac{\partial}{\partial x_j}\left[\left(\frac{\nu}{\mathrm{Pr}} + \frac{\nu_t}{\mathrm{Pr}_t}\right)\frac{\partial \bar{T}}{\partial x_j}\right], \tag{2.2.4}$$

where a bar denotes a quantity that has been spatially filtered and ν_t is an unknown quantity connected to the sgs scales and must therefore be modelled. This unknown quantity will be discussed in the section about the numerical method.

2.3 Treatment of streamwise periodic variations

An internal flow is a flow that is contained within some solid surroundings. This limits the development of boundary layers. For internal flow, in the $\hat{x}_1$ direction through a pipe with non-varying cross sectional area is called fully developed when the conditions

$$\frac{\partial u_i}{\partial x_1} = 0 \tag{2.3.1}$$

are fulfilled and corresponds to flow far from the entrance region [8]. When the cross sectional area varies this condition can no longer be fulfilled and special attention is needed. Modeling flow in a pipe with variational cross sectional area in a period of length L, and that is far from the entrance region, can be done by assuming a periodic behavior in the streamwise direction,

$$u_i(x_1, x_2, x_3) = u_i(x_1 + L, x_2, x_3). \tag{2.3.2}$$

This replaces the criterion $\partial u_i/\partial x_1 = 0$ for a fully developed flow in a straight pipe. Fixing a position x_1' and mapping the interval $[x_1', x_1' + L]$ in the $\hat{x}_1$ direction to the interval $[0, L]$, with boundary conditions

$$u_i(0, x_2, x_3) = u_i(L, x_2, x_3) \tag{2.3.3}$$

then provides a suitable computational domain. This domain will be called a section.

There is a need to specially treat the pressure. For perpetual fluid motion in a certain direction there is necessarily a pressure gradient driving the fluid. Hence the pressure must decrease when going from one section to the next downstream. Since the sections are equivalent it is expected that the pressure distributions in two different sections have the same shape. This can be expressed as

$$p(x_1, x_2, x_3) - p(x_1 + L, x_2, x_3) = p(x_1 + L, x_2, x_3) - p(x_1 + 2L, x_2, x_3). \tag{2.3.4}$$

Now define β as the pressure drop over an interval $[x_1, x_1 + L]$ divided by L

$$\beta = \frac{p(x_1, x_2, x_3) - p(x_1 + L, x_2, x_3)}{L}. \tag{2.3.5}$$

The resulting pressure field can then be expressed as

$$p(x_1, x_2, x_3) = -\beta x_1 + \mathscr{P}(x_1, x_2, x_3) \tag{2.3.6}$$

where $-\beta x_1$ is the overall pressure drop driving the fluid, and $\mathscr{P}$ is a pressure field responsible for local variations in the fluid flow. Inserted into (2.2.3) this gives the governing momentum equations as

$$\frac{\partial \bar{u}_i}{\partial t} + \frac{\partial \bar{u}_i \bar{u}_j}{\partial x_j} = \frac{1}{\rho}\beta\delta_{1j} - \frac{1}{\rho}\frac{\partial \bar{P}}{\partial x_j} + \frac{\partial}{\partial x_j}\left[(\nu + \nu_t)\frac{\partial \bar{u}_i}{\partial x_j}\right], \tag{2.3.7}$$

where δ_{1j} is the Kronecker delta with one index fixed.

A similar treatment works for the temperature, with the difference that the temperature is expected to rise downstream if there is a constant wall heat flux into the fluid. This gives the condition

$$T(x_1 + L, x_2, x_3) - T(x_1, x_2, x_3) = T(x_1 + 2L, x_2, x_3) - T(x_1 + L, x_2, x_3). \tag{2.3.8}$$

Defining σ as

$$\sigma = \frac{T(x_1 + L, x_2, x_3) - T(x_1, x_2, x_3)}{L} \tag{2.3.9}$$

enables the separation into

$$T(x_1, x_2, x_3) = \sigma x_1 + T'(x_1, x_2, x_3) \tag{2.3.10}$$

where T' is the periodic part. Sigma may be determined by the expression

$$\sigma = \frac{Q}{\dot{m} c_p L} \tag{2.3.11}$$

where Q is the rate of added heat, $\dot{m}$ is the mass flow and c_p is the specific heat [1]. This together with (2.2.4) finally gives the energy equation in a periodic setting as

$$\frac{\partial \bar{T}'}{\partial t} + \frac{\partial \bar{u}_j \bar{T}'}{\partial x_j} = -\sigma \bar{u}_1 + \frac{\partial}{\partial x_j}\left[\left(\frac{\nu}{\mathrm{Pr}} + \frac{\nu_t}{\mathrm{Pr}_t}\right)\frac{\partial \bar{T}'}{\partial x_j}\right]. \tag{2.3.12}$$

Chapter 3

Numerical Method

The first section gives an overview of the Finite Volume Method used in the present study.

3.1 The Finite Volume Method

The equations (2.3.7) and (2.3.12) all take the form of a general scalar transport equation [6]

$$\frac{\partial \rho \phi}{\partial t} + \frac{\partial \rho u_j \phi}{\partial x_j} = \frac{\partial}{\partial x_j}\left[\Gamma \frac{\partial \phi}{\partial x_j}\right] + S, \tag{3.1.1}$$

ϕ being the scalar quantity that is transported, Γ is a function describing material properties and S is a source term. Let this equation be defined on a bounded domain Ω with a structured meshing consisting of control volumes with one centered node called P. The structure of the control volumes is shown in figure 3.1. The control volumes are numbered by $\{i, j, k\}$ in a right handed system, and the faces are labeled with lower case letters e(ast), w(est), n(orth), s(outh), h(igh) and l(ow).

This labeling is also used for neighbouring nodes using capital letters E, W, N, S, H and L. Multiply the transport equation with a testfunction φ_I that is constant over a control volume I in the mesh, called Ω_I and zero elsewhere. Integration over the time interval $\Delta t = t_2 - t_1$ and Ω gives

$$\int_{t_1}^{t_2} \int_{\Omega_I} \left(\frac{\partial \rho \phi}{\partial t} + \frac{\partial \rho u_j \phi}{\partial x_j} \right) d\Omega dt = \int_{t_1}^{t_2} \int_{\Omega_I} \left(\frac{\partial}{\partial x_j}\left[\Gamma \frac{\partial \phi}{\partial x_j}\right] + S \right) d\Omega dt \tag{3.1.2}$$

where the testfunction limits the spatial integration to the specific cell Ω_I. There are two divergences in this equation. Using the divergence theorem

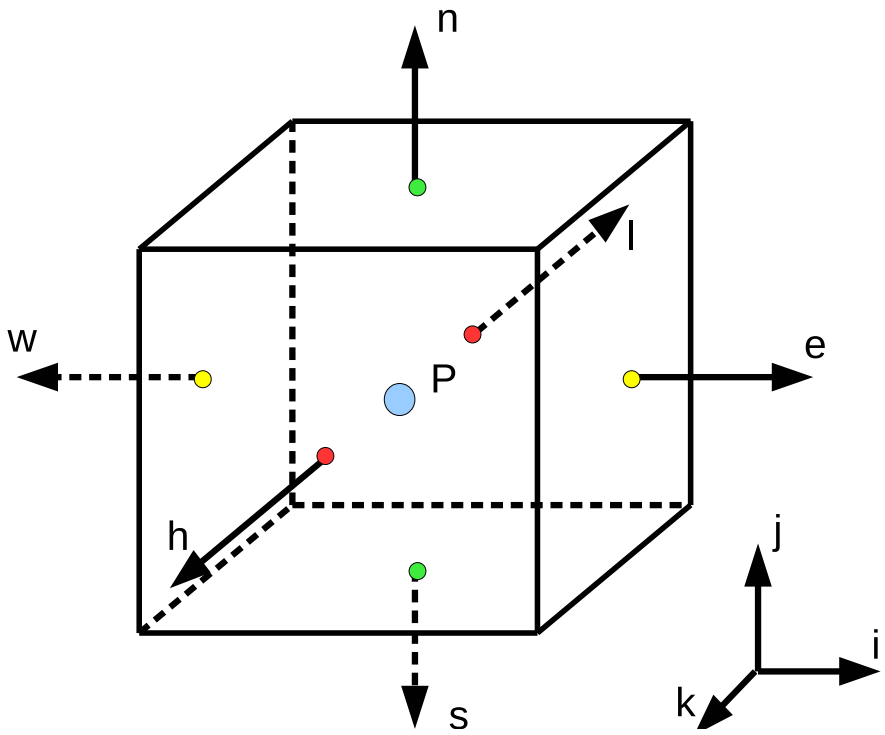

Figure 3.1: Structure of the control volumes

results in

$$\int_{t_1}^{t_2}\int_{\Omega_I}\frac{\partial\rho\phi}{\partial t}d\Omega dt+\int_{t_1}^{t_2}\int_{\partial\Omega_i}\rho u_j\phi\hat{n}_j ds dt=\int_{t_1}^{t_2}\int_{\partial\Omega_I}\Gamma\frac{\partial\phi}{\partial x_j}\hat{n}_j ds dt + \int_{t_1}^{t_2}\int_{\Omega_i}S d\Omega dt \quad (3.1.3)$$

where $\hat{n}_j$ is the outbound normal to the cell and ds is the surface element. The surface integrals are of the form

$$\int_{\partial\Omega}\Lambda_j\hat{n}_j ds. \quad (3.1.4)$$

To evaluate them a discretisation is introduced. The value of Λ is then represented by a single value over the whole face, denote this value as $[\Lambda]_e$ for the value at the east face, $[\Lambda]_n$ for the north one etc. Let A_e be the area of the east face and so on for the other faces. Then the integral is approximated

as

$$\int_{\partial\Omega} \Lambda_j \hat{n}_j ds = [\Lambda]_e A_e + [\Lambda]_w A_w + [\Lambda]_n A_n + [\Lambda]_s A_s + [\Lambda]_h A_h + [\Lambda]_l A_l \equiv \sum_k [\Lambda]_k A_k \tag{3.1.5}$$

where $k \in \{e, w, n, s, h, l\}$. Now equation (3.1.3) can be written as

$$\int_{t_1}^{t_2} \int_{\Omega_I} \frac{\partial \rho\phi}{\partial t} d\Omega dt + \int_{t_1}^{t^2} \sum_k [\rho u_j \hat{n}_j^{(k)} \phi]_k A_k dt = \int_{t_1}^{t^2} \sum_k \left[\Gamma \frac{\partial \phi}{\partial x_j} \hat{n}_j^{(k)}\right]_k A_k dt + \int_{t_1}^{t_2} \bar{S} dt \tag{3.1.6}$$

where $\hat{n}_j^{(k)}$ is the outbound normal to surface k and $\bar{S}$ is some approximation of the volume integral over the source. Assume that

$$[\rho u_j \hat{n}_j^{(k)} \phi]_k = [\rho u_j \hat{n}_j^{(k)}]_k \phi_k \tag{3.1.7}$$

is a valid separation for the terms in the first sum and

$$\left[\Gamma \frac{\partial \phi}{\partial x_j} \hat{n}_j^{(k)}\right]_k = \Gamma_k \left[\frac{\partial \phi}{\partial x_j} \hat{n}_j^{(k)}\right]_k \tag{3.1.8}$$

for the second. The terms in the first sum describes convective fluxes of quantity ϕ over the faces and the terms in the second sum describe diffusive transport over the faces. Note that ϕ_k can be determined by interpolation from appropriate node values. In the case of linear interpolation

$$\phi_e = f_e \phi_E + (1 - f_e)\phi_P, \tag{3.1.9}$$

where f_e is an interpolating factor determined from the geometry, gives the value of ϕ on the east face of node P. Using the assumption about separation the discretised equation

$$\int_{\Omega_I} \left[\int_{t_1}^{t_2} \frac{\partial \rho\phi}{\partial t} dt\right] d\Omega + \int_{t_1}^{t^2} \sum_k [\rho u_j \hat{n}_j^{(k)}]_k \phi_k A_k dt = \int_{t_1}^{t^2} \sum_k \Gamma_k \left[\frac{\partial \phi}{\partial x_j} \hat{n}_j^{(k)}\right]_k A_k dt + \int_{t_1}^{t_2} \bar{S} dt. \tag{3.1.10}$$

can be written and is an equation over one specific control volume. To proceed it is necessary to introduce discretisation schemes to treat the different terms involving differentiation and to handle the time integration. These schemes produces algebraic relations between node values, both spatial and temporal, and then couple different control volumes into one sparse algebraic equation system. Ignoring time at the moment, to discretise expressions like (3.1.7) and (3.1.8) a scheme expressing a relation between the node P of the control volume and neighbouring nodes is introduced. This scheme describes contribution due to convection and diffusion over the cell faces. To evaluate integrals in time it is important to consider at what times the discretised quantities involved are taken. Time integration is of the form

$$\int_{t_1}^{t_2} \phi_P \, dt. \tag{3.1.11}$$

A general approach, introducing a parameter $\theta \in [0, 1]$, can be formulated as

$$\int_{t_1}^{t_2} \phi_P dt = \left(\theta \phi_P^{(2)} + (1-\theta)\phi_P^{(1)}\right) \Delta t, \tag{3.1.12}$$

where the superscript denotes a value at time t_1 or t_2 [6]. Choosing $\theta = 0$ gives an approximation that only depends on a previously calculated value, this approach is called explicit. $\theta = 1$ gives an approximation dependent on an unknown value at time t_2. This approach is called fully implicit. $\theta = 1/2$ gives an approximation with a mix between an unknown value at time t_2 and a known value at t_1 both with a weight of $1/2$. This is called the Crank-Nicolson scheme and has the adavantage of beeing of second order accuracy in time [6].

3.2 The computational mesh

When solving an algebraic system the order of complexity gives an estimate on the relative computational time [9]. For a serial solution method the number of computational cells sets a limit on how fast the system can be solved. Hence there is lot to gain if the number of cells can be reduced. A possibility to reduce the number of cells is if there are symmetries in the problem that can be used to reduce the size of the domain. In the case of fully developed flow in a pipe there are two such symmetries, one in the streamwise direction and one in the azimuthal direction. Another possibility to control the number of computational cells is to stretch the mesh so that it has a high density where there is a need of higher resolution in the solution

and low density where required resolution is lower [6].

The case of symmetry in the streamwise direction has been touched upon in section 2.3. This symmetry opens the possibility to decrease the computational domain in the streamwise direction by controlling the periodic boundary condition in the streamwise direction by cutting of, and recirculating the computed flow after a certain length. The azimuthal symmetry can be used to reduce the computational domain by only consider a pie cut of the pipe and identify the computed flows at the azimuthal boundaries. As long as the influence in the azimuthal direction doesn't self interfere a smaller angle of the pie cut can be considered.

Using these conditions a computational mesh type like the one in figure 3.2 can be used. Here the domain is a 90° pie cut through a straight pipe with x as the streamwise direction. The curved solid pipe wall and the other surfaces consists of cyclic boundaries. The mesh is stretched from the solid wall toward the centerline to gain a higher resolution near the inner wall, where better resolution is needed [6]. Figures 3.3 and 3.4 (page 17) depicts a cut through the x-y plane respectively a cut at the y-z plane boundary in the same computational mesh.

Figures 3.5 (page 18), 3.6 and 3.7 (page 21) show a computational mesh with corrugations.

The mesh in the case of a straight pipe is coded directly into the solver. In the case of a corrugated pipe the mesh is constructed with the help of the code G3DMESH. Notice that the computational meshes are constructed as boundary fitted coordinates so that they follows the boundaries as smoothly as possible.

3.3 Boundary conditions

At the solid wall no-slip boundary conditions are used for the velocity so all velocity components are set to zero at the wall. For the temperature equation a constant heat in-flux is prescribed.

At the centerline symmetry boundary conditions are used, the radial velocity component are set to zero and all other quantities, including the temperature, are set to have zero flux over the centerline.

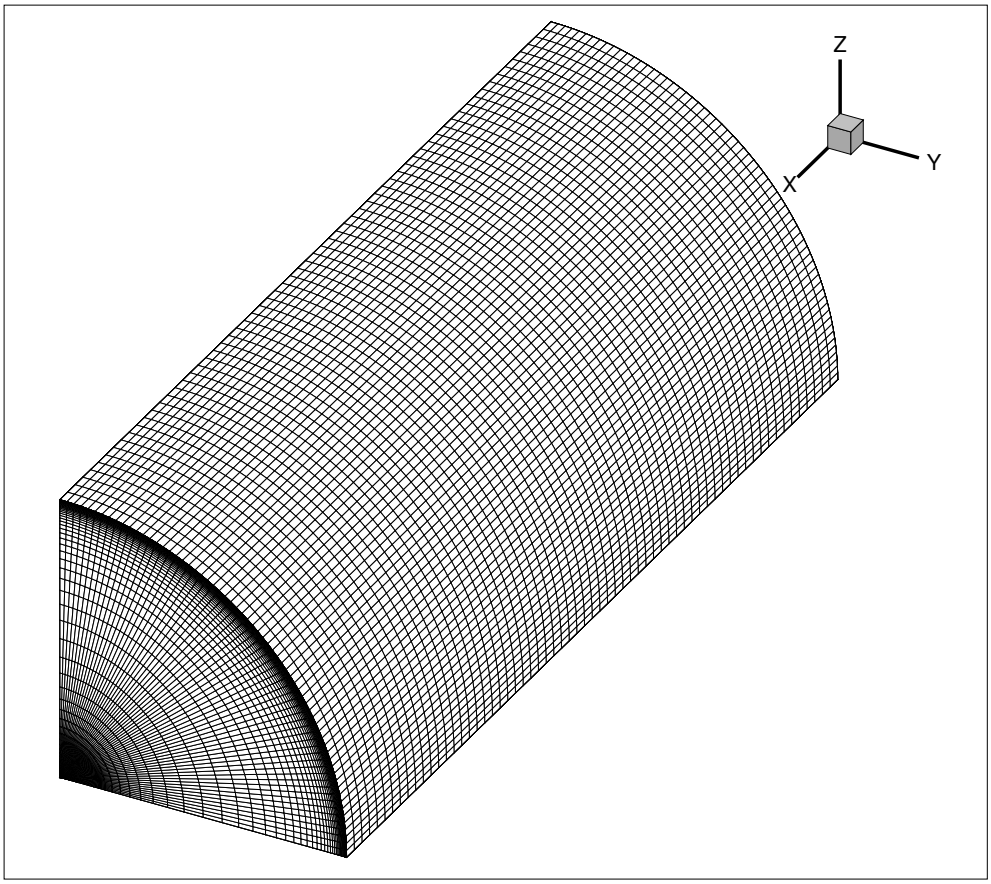

Figure 3.2: Computational mesh for a straight pipe

At cyclic boundaries the computational values are identified with the corresponding cyclic boundary producing an interlacing that freely transports between the connected boundaries.

3.4 LES and the WALE model

The present work use LES-filtered equations that are described in section 2.2. As model for the sgs stress tensor the WALE model (abbreviation for Wall-Adapting Local Eddy-viscosity) is used [10]. In this model the connection between the resolved scales and the subgrid scales is modelled by a

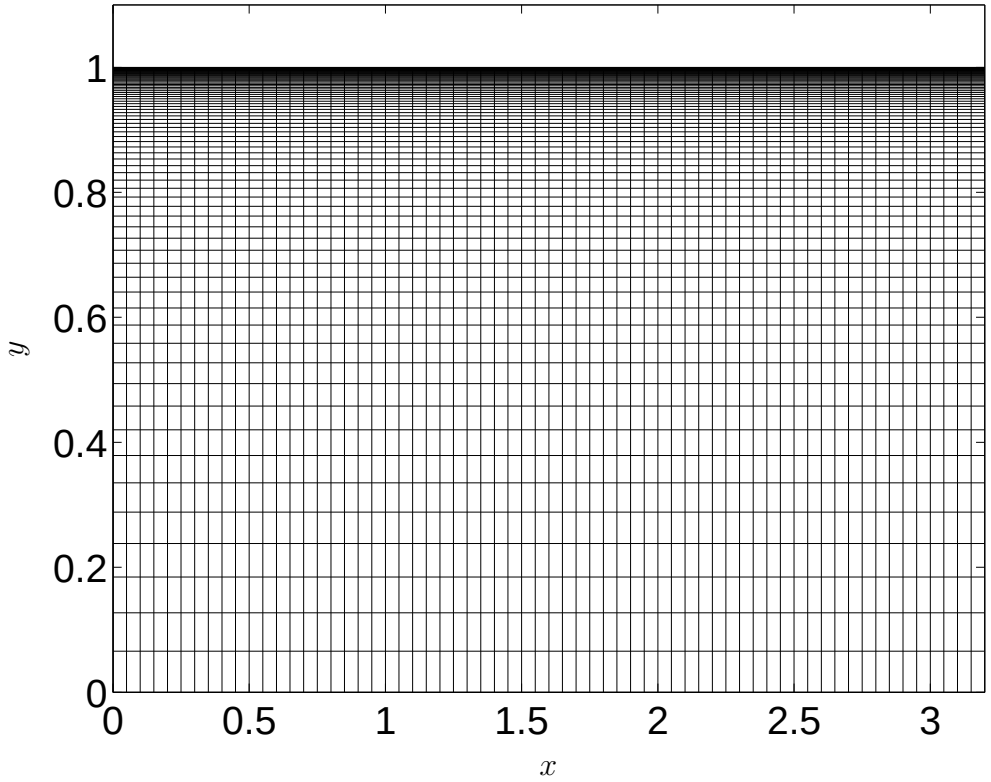

Figure 3.3: Computational mesh of straight pipe, cut through the x-y plane

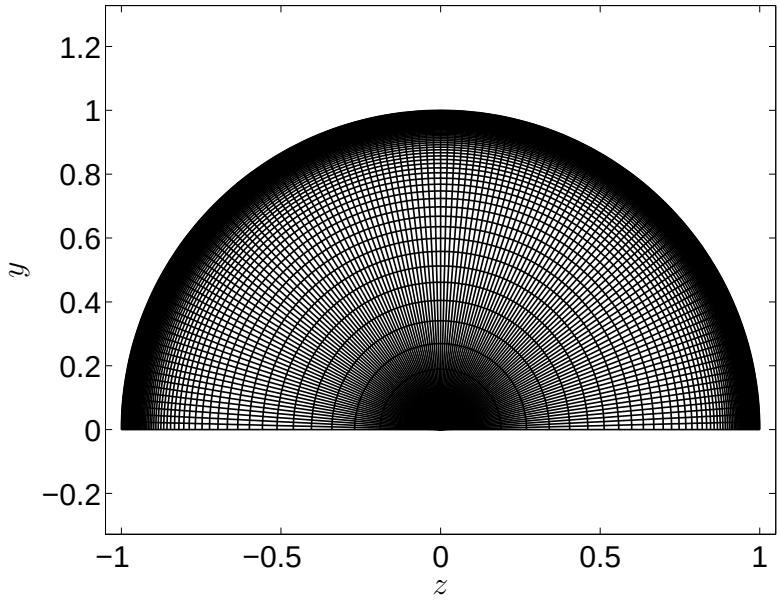

Figure 3.4: Computational mesh of straight pipe, inlet y-z plane

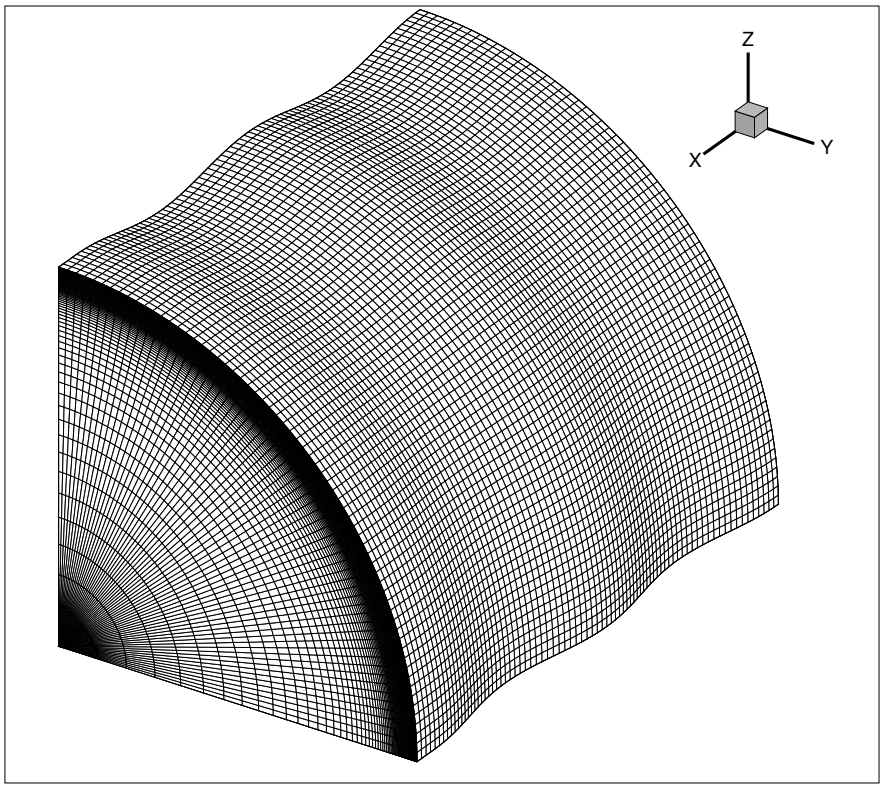

Figure 3.5: Computational mesh for a corrugated pipe

turbulent Eddy-viscosity ν_t according to

$$\nu_t = \Delta_s^2 \frac{(S_{ij}^d S_{ij}^d)^{3/2}}{(\bar{S}_{ij}\bar{S}_{ij})^{5/2} + (S_{ij}^d S_{ij}^d)^{5/4}} \tag{3.4.1}$$

where

$$\Delta_s = C_w V^{1/3}, \tag{3.4.2}$$

C_w is a numerical constant, V is the cell volume,

$$S_{ij}^d = \frac{1}{2}\left[\left(\frac{\partial \bar{u}_i}{\partial x_j}\right)^2 + \left(\frac{\partial \bar{u}_j}{\partial x_i}\right)^2\right] - \frac{1}{3}\delta_{ij}\left(\frac{\partial \bar{u}_k}{\partial x_k}\right)^2 \tag{3.4.3}$$

and finally

$$\bar{S}_{ij} = \frac{1}{2}\left(\frac{\partial \bar{u}_i}{\partial x_j} + \frac{\partial \bar{u}_j}{\partial x_i}\right) \tag{3.4.4}$$

is the ordinary stress tensor based in the resolved scales. This expression for the turbulent viscosity can now be used in equation 2.3.7 and 2.3.12 that finally closes the equation system.

3.5 The β and σ parameters

The β parameter introduced in section 2.3 acts as a source driving the fluid. This parameter can be set to a fixed value that multiplied by the volume balances the wall shear stress when the flow becomes fully developed. In the case of a straight pipe it is possible to prescribe $\beta = 2$ so that the total wall shear stress equals one. This is done for the straight pipe in the present study. There is also the possibility to continuosly adapt the value of β to achieve a prescribed mean flow. This is done in the case of a corrugated pipe to achieve a mean flow of one.

The σ parameter acts as a heat sink in the energy equation. It is determined so that it extracts the same amount of energy that the constant wall heat flux deposits per unit time into the system. This is necessary since the temperature is recycled in the computational system through the cyclic boundary in the streamwise direction. In reality, the temperature is advected further downstream when it leaves the domain.

3.6 The Finite Volume solver

To solve equations like (3.1.10) one usually uses a solver of some type, typically written in a fast compiled language such as Fortran or C/C++. The present study uses an implementation of the CALC-BFC solver [11], written in Fortran and developed at the division of Fluid Dynamics, Chalmers University of Technology. The code is capable of handling incompressible unsteady turbulent recirculating flows together with the energy equation. The code uses structured grids with Boundary Fitted Coordinates (BFC), suitable for geometries where boundaries varies in a nonlinear fashion. All computational variables are stored collocated in a central node of each control volume in a global Cartesian coordinate system.

To handle the velocity-pressure coupling the solver uses a fractional step algorithm [12]. The algorithm involves solving a Poisson equation and this is done using multigrid technique.

3.7 Discretisation schemes

In the present study, the central differencing scheme is used to discretise the momentum equations and the hybrid scheme is used to disktretise the energy equation. The Crank-Nicolson scheme is used for time discretisation [6].

3.8 The simulation methology

A simulation is conducted in the following steps.

1. The computational mesh is created and all parameters are set.
2. From a suitable start guess the system is iterated until the flow is fully developed and the flow characteristics are then saved.
3. With the saved flow a new run is started and iterated for 10.000 timesteps under fully developed conditions.
4. The flow characteristics are sampled for another 10.000 timesteps where the characteristics are averaged over the azimuthal direction and time.

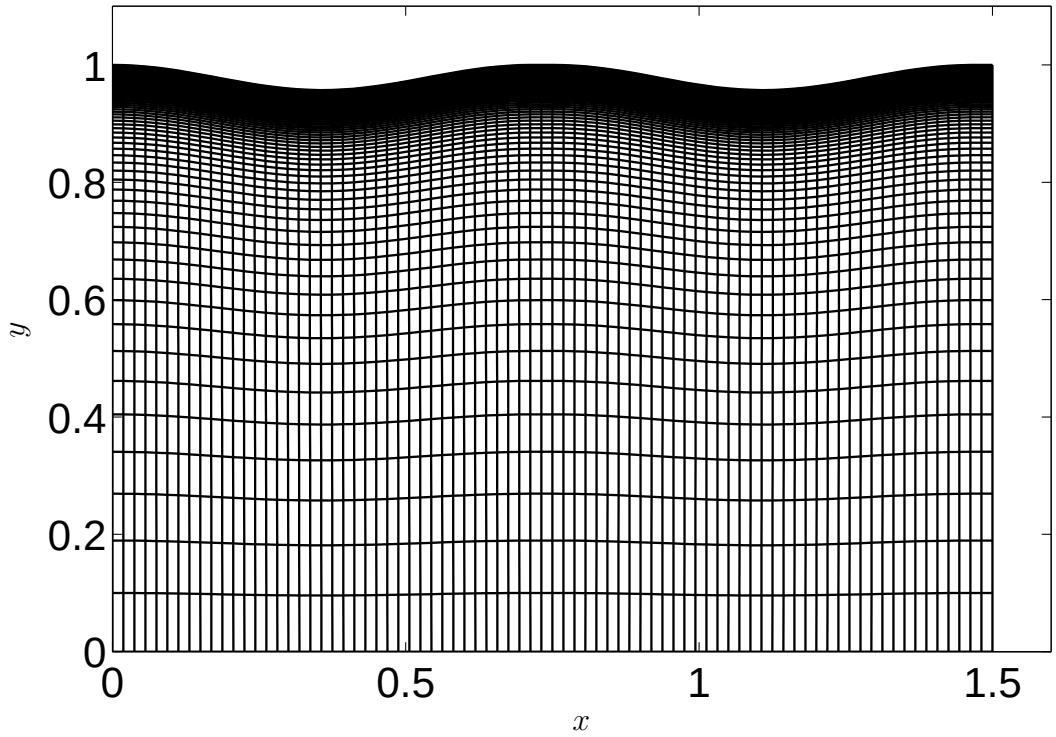

Figure 3.6: Computational mesh of corrugated pipe with reduced number of cells, cut through the x-y plane

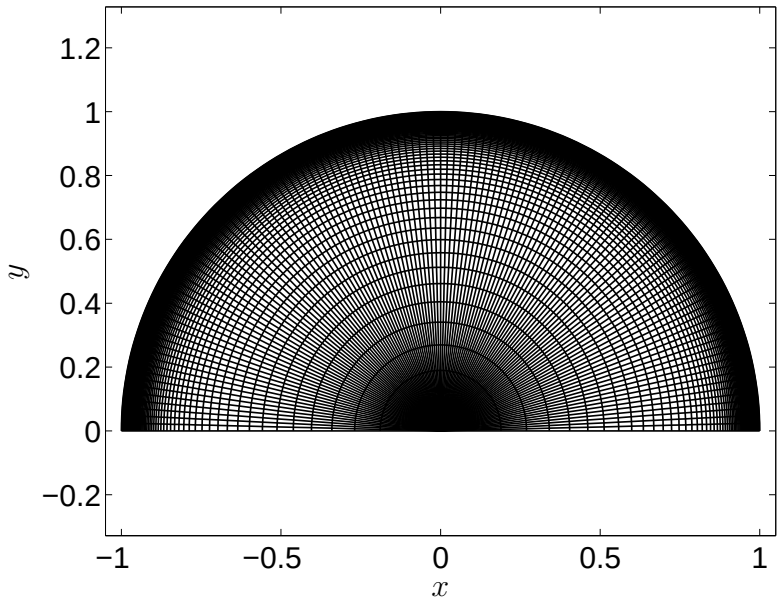

Figure 3.7: Computational mesh of a corrugated pipe, inlet y-z plane

Chapter 4

Results

4.1 Simulation of a straight pipe

To verificate the code and for comparison with the corrugated geometry, a simulation case of a straight pipe with a fluid of Prandtl number 3.5 and density $\rho = 1$ was set up. The specific heat was set to $c_p = 1$ and a constant heat flux of $q = 10^{-3}$ was set at the wall. The driving force in the simulation was set so that a wall friction of one whould be accomplished in average, this corresponds to setting a β=2 as a driving force. The Reynolds number was chosen as $Re_\tau = 395$, based on the wall friction. The computational domain was set to a radius of $R = 1$ and a length $l = 3.2$. The grid was exponentially stretched in the radial direction from the wall towards the center with a stretching factor of 1.07. In the radial direction 80 cells was used and the near wall cell was set to a width of $\Delta y^+ = 0.12$. The number of cells in the azimuthal direction was set so that the azimuthal spacing along the pipe wall was $\Delta z^+ = 9.7$ with a uniformally spaced grid.

Figure 4.1 shows convergence of the Nusselt number for increasing the computational domain together with two empiric correlation functions with the calculated bulk velocity as input. It can be seen that the change in Nusselt number between a domain of 180° and 360° is negligable, hence a computational grid of 180° is reasonable. It is here noted that the resulting Nusselt number for the straight pipe is $\langle Nu_{str} \rangle = 76.9$. The resulting velocity profile for a simulation with a domain of 180° is shown in figures 4.2 and 4.3 in ordinary and wall coordinates respectively. The mean velocity is calculated to be $u_b = 18.0$. The profile compares well to the log law $u^+ = \ln y^+ / 0.41 + 5.5$ and the behavior in the viscous sublayer is close to $u^+ = y^+$.

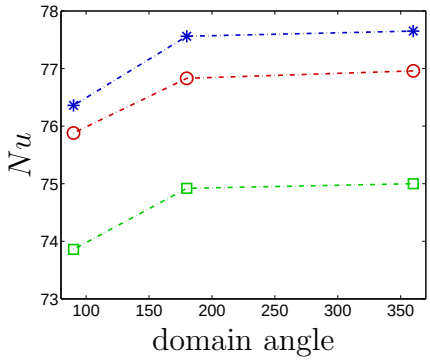

Figure 4.1: Convergence of Nusselt number for domain of 90°, 180° and 360° (red circles) together with Gnielinski (blue stars) and Dittus-Boelter (green squares) correlations

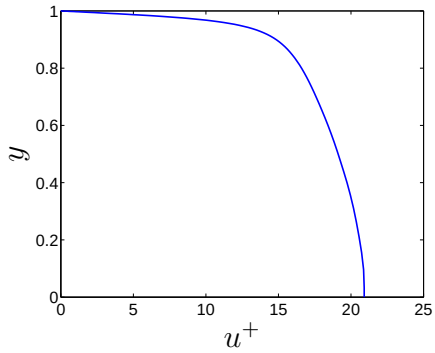

Figure 4.2: Velocity profile for the straight pipe

Defining a dimensionless pressure drop as $\Delta p^* = \beta/\rho u_b^2$, gives in the straight pipe case $\Delta p_1^* = 6.18 \times 10^{-3}$.

Figure 4.4 shows the temperature profile up until some distance from the wall. Figure 4.5 shows both the viscous heat flux $-\nu/Pr \times \partial\langle T\rangle/\partial y$ and the turbulent heat flux $-\langle v_r' T'\rangle$ in the radial direction.

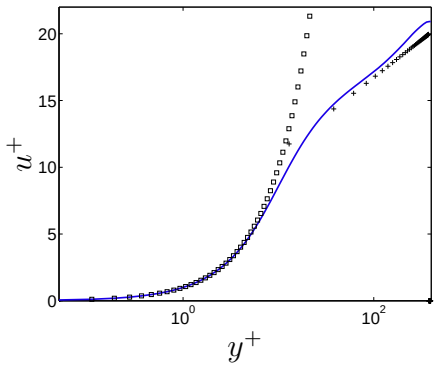

Figure 4.3: Blue solid line shows the velocity profile in wall coordinates. $\square : u^+ = y^+$; $* : u^+ = \ln y^+ / 0.41 + 5.5$

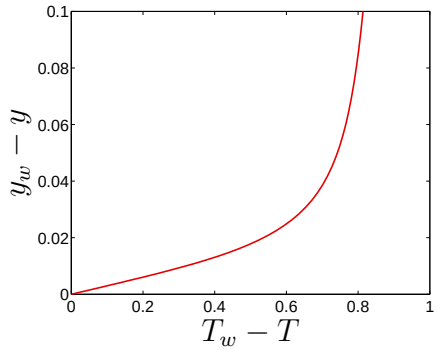

Figure 4.4: Temperature profile for the straight pipe

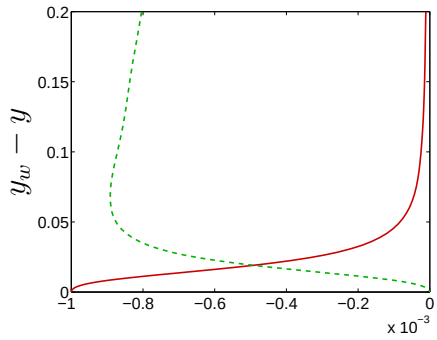

Figure 4.5: Viscous heat transfer (red solid) and turbulent heat transfer (green dashed) in the radial direction for a straight pipe

4.2 Simulation of the corrugated pipe

For the simulation of the corrugated pipe a computational domain with dimensions shown in figure 4.6 are used. The domain contains two full corrugations with one full corrugation centered in the domain ranging from $x = 0.35$ to $x = 1.1$ peak to peak. The number of computational cells are chosen as $n_x = 80$, $n_r = 80$ and $n_\varphi = 128$ in the streamwise, radial and azimuthal directions respectively This results in a total of 819200 computational cells. This choice gives the same size of the cells at the wall in the radial and azimuthal direction as in the case of the straight pipe.

In the present simulation a target bulk velocity of $u_b = 1$ is chosen. To achieve this a continuous change of the β-parameter is made to adapt the driving force towards the target bulk velocity. For the present simulation the mean value of this parameter was $\bar{\beta} = 1.34 \times 10^{-2}$. The Reynolds number is chosen as $Re_R = 10^4$ with lengthscale $R = 1$ corresponding to the pipe radius. The density is assumed to be $\rho = 1$ so that the kinematic viscosity is expressed as $\nu = Re_d^{-1} = 10^{-4}$. Further the specific heat is assumed to be $c_p = 1$ and the Prandtl number is set to $Pr = 3.5$. The constant heat flux condition at the wall is sett to $q = 10^{-3}$.

The present simulation was initiated from a prior velocity field with a bulk velocity of at least precission $u_b = 1.0 \pm 0.05$. The simulation was made by initiating a constant temperature field and further evolving the Navier-Stokes and energy equation system for 10.000 time steps. Time series of the velocities, temperature and combinations of these quantities where then sampled during the evolution of another 10.000 time steps.

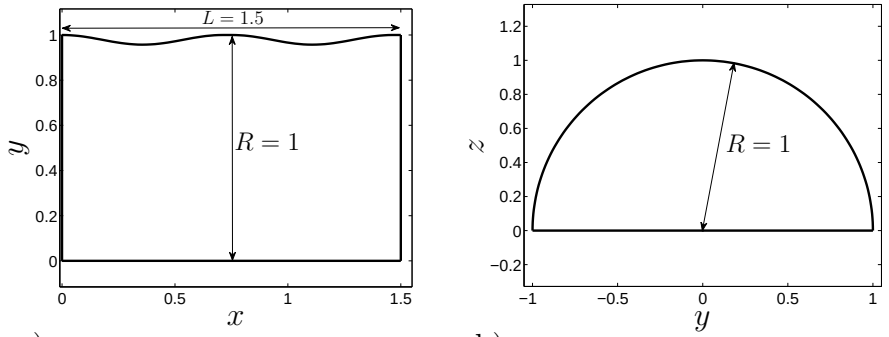

a) b)

Figure 4.6: a) Dimensions of the computational domain in the slice $z = 0$ b) Dimensions of the computational domain in the slice $x = 0$

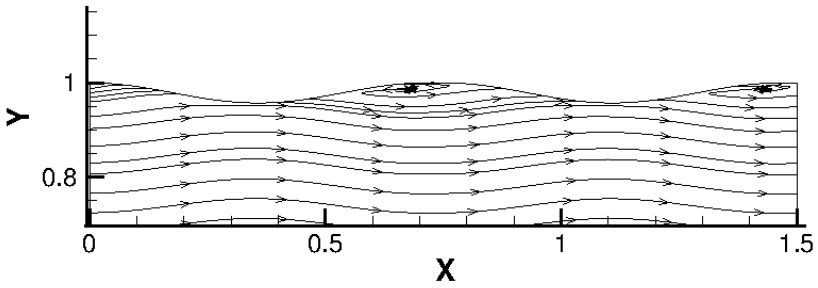

Figure 4.7: Averaged velocity streamlines near the upper wall

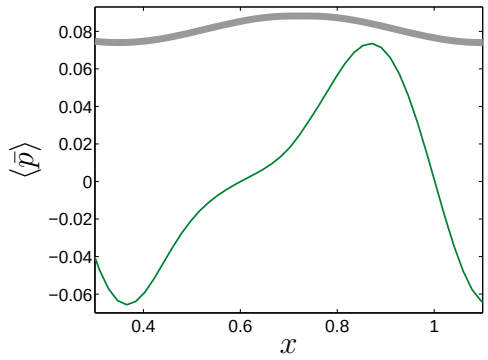

Figure 4.8: Periodic mean wall pressure over a corrugation. The thick grey line shows the corrugation profile

4.3 Flow field characterisation

Since both the bulk velocity and density is chosen as 1, the dimensionless pressure drop Δp_2^* is equal to the resulting β parameter, $\bar{\beta} = 1.34 \times 10^{-2}$. Comparing to the straight pipe case the pressure drop then increases with a factor $\Delta p_2^*/\Delta p_1^* = 2.2$.

In figure 4.7 the streamlines, averaged over the azimuthal direction and time, are shown. Focusing on the central corrugation a flow separation can be observed near $x = 0.5$ and later rattached near $x = 0.8$ creating a small re-circulation bubble at the bottom of the corrucation. The resulting periodic

mean pressure near the wall is shown in figure 4.8. It can be seen that near the wall, the pressure is negative for negative slope of the corrugation and possitive for possitive slope of the corrugation (seen in the normal direction of the wall) with a maximal value near the reattachment point, which is close to the point of maximal slope of the wall. The minimum is located in the region where the corrugation slope is zero at the top of a corrugation. The pressure changes sign at the bottom of a corrugation where the slope is zero.

Figure 4.9 shows the resulting friction coefficient over one corrugation and the dashed line shows the friction coefficient for a straight pipe. The friction coefficient is greater than the corresponding straight pipe up until $x = 0.42$ and after $x = 0.87$. The peak value is $C_{f,max} = 0.022$ which is 3.7 times the value for a straight pipe. The coefficient becomes negative in the intervall $x = 0.5$ to $x = 0.8$ in accordance with the recirculation.

The left plot in figure 4.10 shows the averaged velocity profiles of the u component over the wall normal direction at different streamwise locations outside the recirculation zone. The right plot shows the location related to the corrugation profile. It is noticed that the velocity profiles have similar behaviour near the wall. Figure 4.11 shows the same as figure 4.10 for the region inside the recirculation zone. It can be seen that the velocity profiles achieves small negative values near the wall of varying magnitudes. Smallest negative magnitudes is found near the separation and reattachment points with larger negative magnitudes in between.

The left plot in figure 4.12 and 4.13 shows turbulent intensity in the radial direction at four different locations outside the recirculation zone and

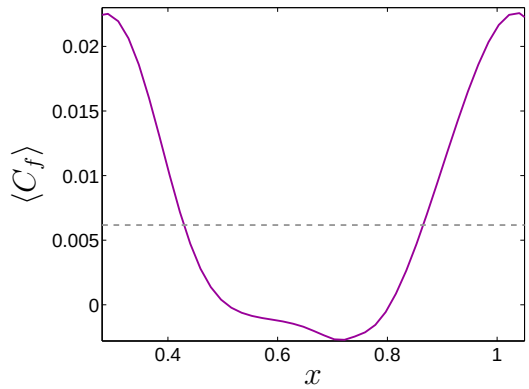

Figure 4.9: Friction coefficient $\langle C_f \rangle$, dashed line shows straight pipe value

inside the recirculation zone respectively. The right plots show the locations of each line relative to the corrugation profile. It can be seen that the intensity is highest in the region after the reattachment point and goes down to about half that intensity inside the recirculation zone.

Figures 4.14 and 4.15 show a similar setting as in the previous plots for the Reynolds shear stress $\langle u'v'_r \rangle$. The Reynold Stress changes behaviour near the separation point where it changes sign close to the wall and accompanied with a smaller magnitude. This seems to a small extent somewhat correlated with the turbulent intensity.

Finally, in figure 4.16 the maximal RMS-values of the three velocity components are shown as functions of the streamwise direction. It is seen that the fluctuations in the components orthogonal to the streamwise direction has a little bit higher fluctuation maxima in the part where the corrugation "rises", that is where the pipe radius decreases. This is where the streamvise fluctuations has its fluctuation maxima more centered relative to the corrugation.

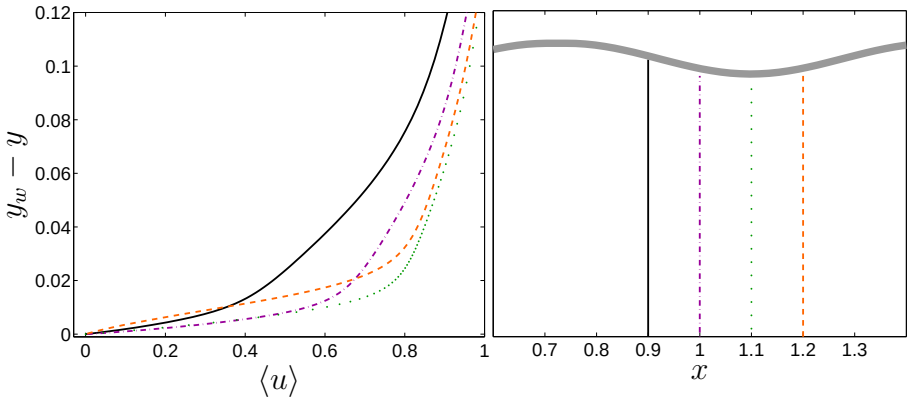

Figure 4.10: Averaged velocity profiles $\langle u \rangle$ outside the recirculation zone at locations $x = 0.9$, $x = 1.0$, $x = 1.1$, $x = 1.2$

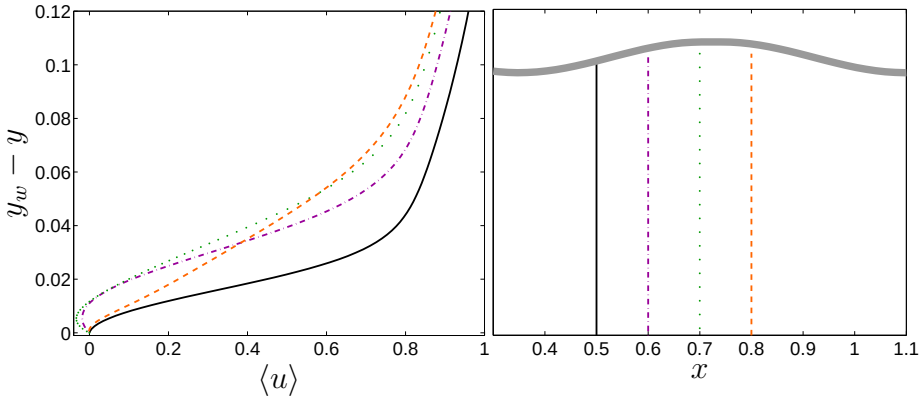

Figure 4.11: Averaged velocity profiles $\langle u \rangle$ inside the recirculation zone at locations $x = 0.5$, $x = 0.6$, $x = 0.7$, $x = 0.8$

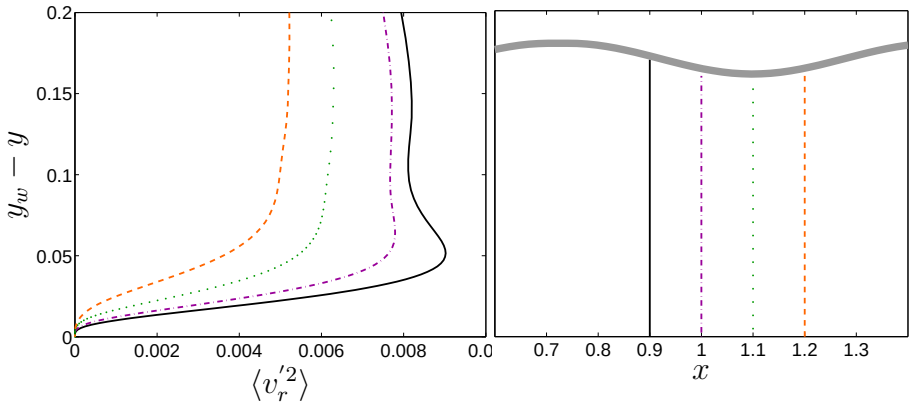

Figure 4.12: Averaged turbulent intensity $\langle v_r'^2 \rangle$ outside the recirculation zone at locations $x = 0.9$, $x = 1.0$, $x = 1.1$, $x = 1.2$

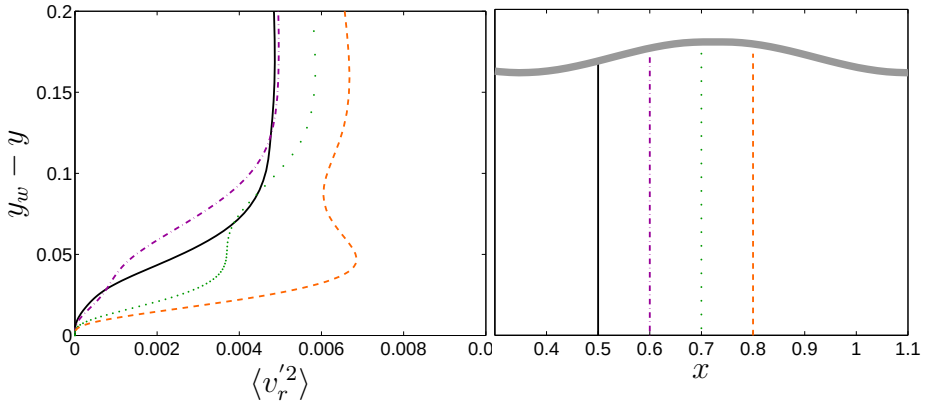

Figure 4.13: Averaged turbulent intensity $\langle v_r^2 \rangle$ inside the recirculation zone at locations $x = 0.5$, $x = 0.6$, $x = 0.7$, $x = 0.8$

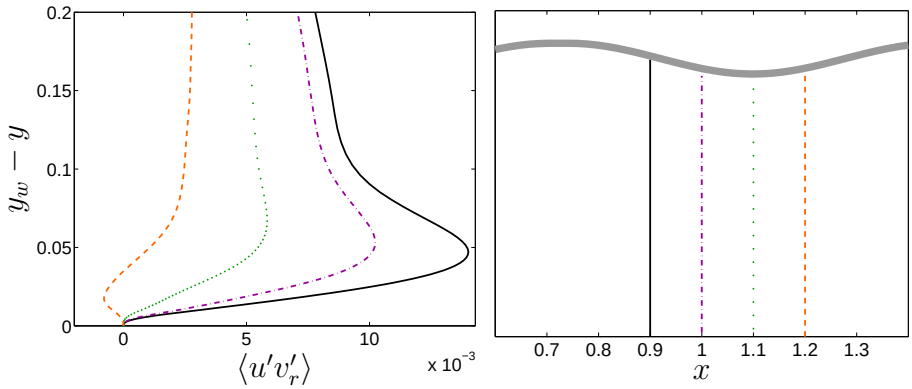

Figure 4.14: Averaged turbulent shear stress $\langle u'v'_r \rangle$ outside the recirculation zone at locations $x = 0.9$, $x = 1.0$, $x = 1.1$, $x = 1.2$

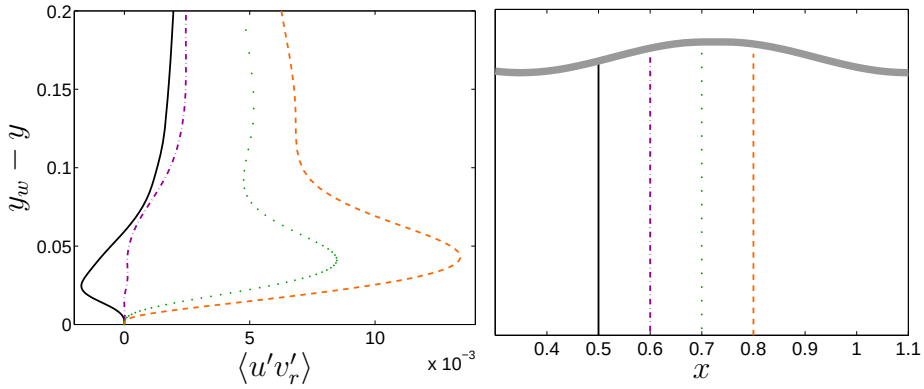

Figure 4.15: Averaged turbulent shear stress $\langle u'v'_r \rangle$ inside the recirculation zone at locations $x = 0.5$, $x = 0.6$, $x = 0.7$, $x = 0.8$

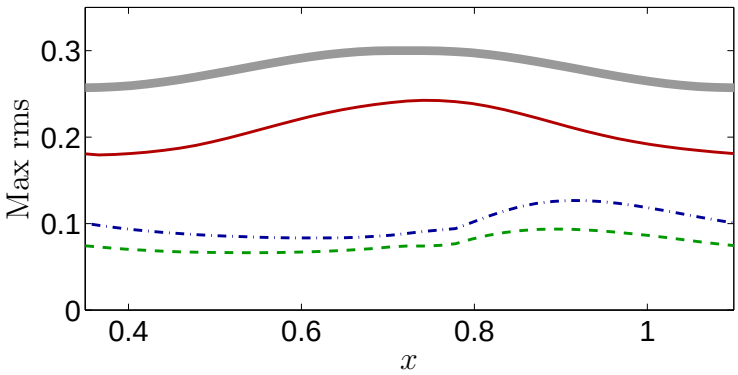

Figure 4.16: Max of $\langle u_{rms} \rangle$ (solid red), $\langle v_{rms} \rangle$ (dashed green) and $\langle w_{rms} \rangle$ (dotted and dashed blue) in the streamwise direction

4.4 Thermal field and heat transfer characterisation

Figure 4.17 shows the periodic wall temperature $\langle T \rangle$ and the local Nusselt number $\langle Nu \rangle$ respectively over one corrugation. The average $\langle Nu \rangle$ over one corrugation was $\langle \bar{N}u \rangle = 95.3$. comparing to the straight pipe case this gives an increasing factor of $\langle \bar{N}u \rangle / \langle Nu_{str} \rangle = 1.24$. Energy accumulates with a peaked temperature value in the intervall $x = 0.4$ and $x = 0.8$, the maximum is located at $x = 0.57$. It is also noted that the minimum is located at $x = 1.0$. This can be compared to the local Nusselt number that drops below the value of a straight pipe in the intervall $x = 0.48$ and $x = 0.70$ with a minimum of 49 at $x = 0.57$ which is 0.64 times the value for a straight pipe. It is also observed that the local Nusselt numbers increase well above the value for a straight pipe up to a value of 137 at $x = 1.0$ close to the peak of the corrugation. This corresponds to a value 1.8 times the value for a straight pipe. This promotes a hypothesis that the accumulated heat is related with the lower performance of the local Nusselt number and the alteration of the Nusselt profile as a whole. Figure 4.18 shows the variation of the maximum of the RMS temperature fluctuations in the streamwise direction and it is seen that this function is somewhat aligned with the temperature peak.

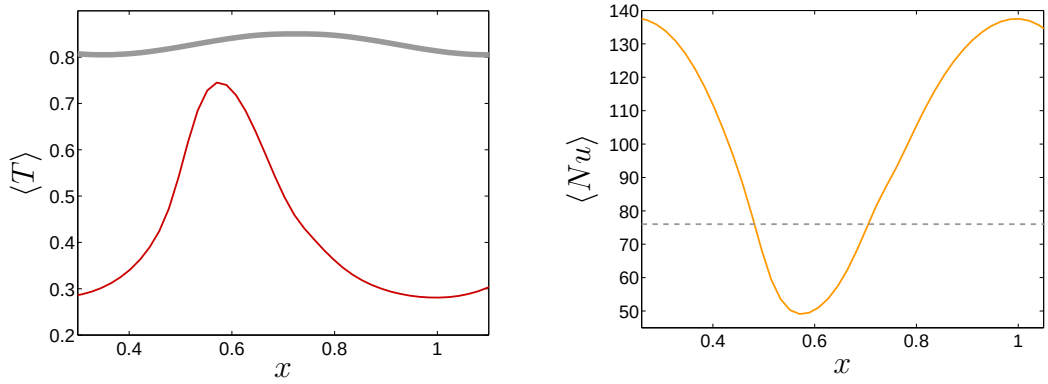

Figure 4.17: Averaged periodic wall temperature $\langle T \rangle$ and Nusselt numbers $\langle Nu \rangle$, dashed lines corresponds to straight pipe, thicker gray line shows corrugation profile

Looking at the temperature profiles for different locations streamwise, it can be seen in figures 4.19 and 4.20 that different low values of the local Nusselt numbers correspond to a higher difference between wall temperature and bulk temperature. This supports the idea that a disturbance of the thermal

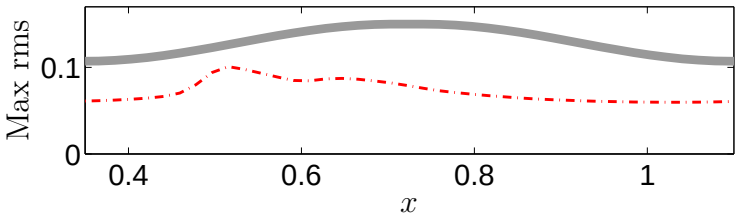

Figure 4.18: Max of $\langle T_{rms} \rangle$ in the streamwise direction

boundary layer is connected with lower values of the local Nusselt numbers.

The viscous heat transfer in the radial direction, defined as $-\frac{\nu}{Pr}\partial\langle T\rangle/\partial y$ is shown in figures 4.21 and 4.22. Once again the region outside the recirculation behaves similar and the viscous heat transfer is quickly reduced from the initial value of 10^{-3} at the wall. In the recirculated area this transfer is maintained also a bit out from the wall. This is consistent with the accumulated heat, a "higher hill" means a higher potential for thermal fluxes. The corresponding turbulent fluxes $-\langle v_r' T' \rangle$, shown in figures 4.23 and 4.24, shows qualitatively two different types of behaviour in the two types of zones. In the zone outside the recirculation the turbulent flux works together with the viscous flux, inforcing transport away from the wall in the proximity. In the first half of the recirculation area the turbulent flux changes direction or maintianes a value close to zero near the wall. The combined effect of these two types of fluxes are shown in figures 4.25 and 4.26. It is shown that the minimum of the local Nusselt numbers are accompanied with a behaviour where the total flux in the radial direction quickly falls toward zero and even changes sign. This happens arround the interval x =0.5-0.6. Figures 4.27 and 4.28 shows the viscous and turbulent flux over one corrugation and focused on the recirculation zone respectively. In the recirculation zone, the heat transfer is disturbed by transport in the streamwise direction closer to the wall. Figure 4.29 shows the magnitude of the viscous and turbulent heat flux in the streamwise direction that is negative, transporting heat against the streamwise direction. Figure 4.30 shows the corresponding magnitude for the radial component for positive values, transporting heat towards the wall. In effect it is seen that the viscous and turbulent transport is partly isolating the earlier mentioned hot spot in the periodic mean temperature. It is here hypothesised that the turbulent fluctuations in effect performes badly in transporting heat away in the viscinity of the temperature hot spot. This results in the geometry influencing the local Nusselt number, giving worse performance then a straight pipe in the region $x = 0.48$ to $x = 0.7$ (figure 4.17 (right)). It is also noted from figure 4.29 that the heat flux goes against

the streamwise direction up until close to $x = 0.57$ where both the periodic wall temperature and the Nusselt numbers have extrema. On the other hand, figures 4.31 and 4.32 shows magnitudes of the x-component of the viscous and turbulent heat flux greater then 6×10^{-3} and the y-component of the viscous and turbulent heat flux is less then 10^{-3}. This indicates that heat is transported past the recirculation zone at a high rate. Figure 4.32 also shows a high transport rate at the wall after the recirculation zone where it is also observed that the local Nusselt number performes better then a straight pipe.

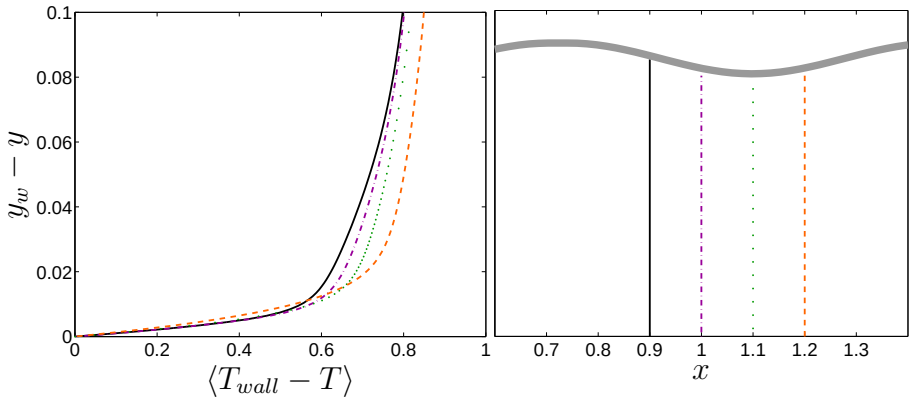

Figure 4.19: Averaged periodic temperature profile $\langle T_{wall} - T \rangle$ outside the recirculation zone at locations $x = 0.9$, $x = 1.0$, $x = 1.1$, $x = 1.2$

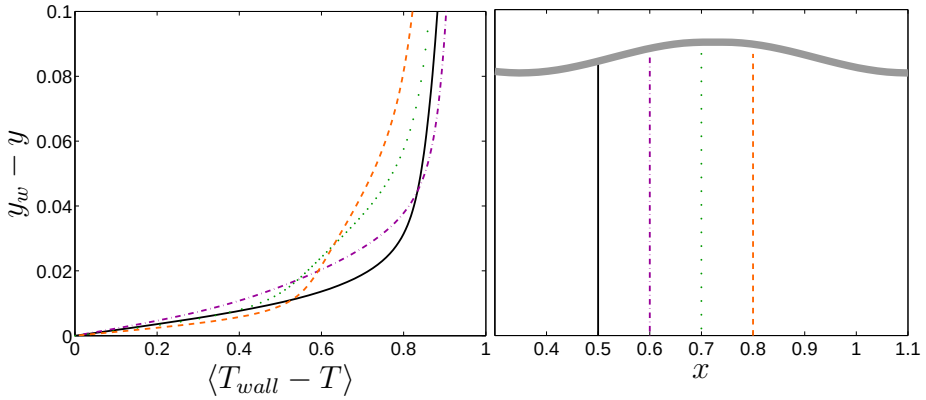

Figure 4.20: Averaged periodic temperature profile $\langle T_{wall} - T \rangle$ inside the recirculation zone at locations $x = 0.5$, $x = 0.6$, $x = 0.7$, $x = 0.8$

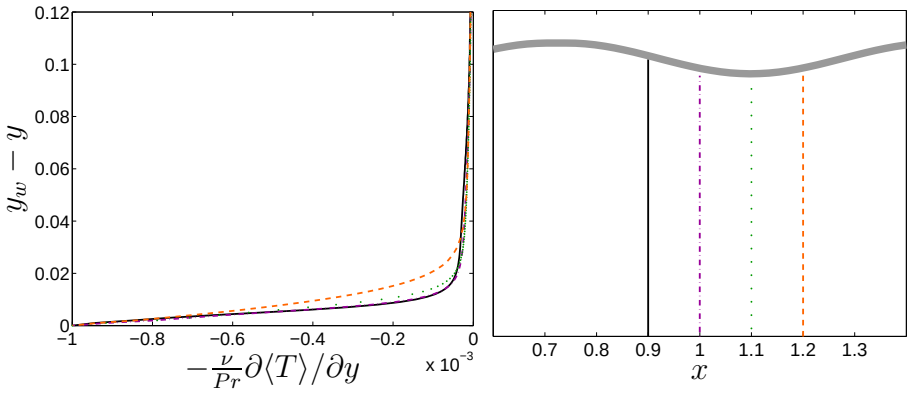

Figure 4.21: Averaged viscous heat flux component $-\frac{\nu}{Pr}\partial\langle T\rangle/\partial y$ outside the recirculation zone at locations $x = 0.9$, $x = 1.0$, $x = 1.1$, $x = 1.2$

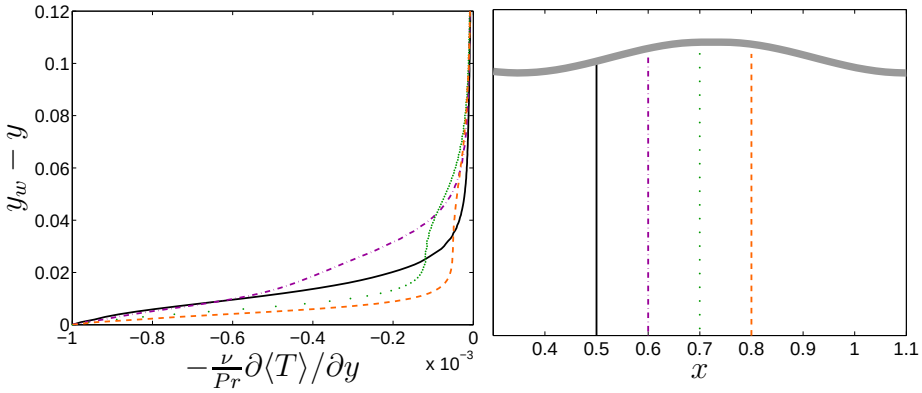

Figure 4.22: Averaged viscous heat flux component $-\frac{\nu}{Pr}\partial\langle T\rangle/\partial y$ inside the recirculation zone at locations $x = 0.5$, $x = 0.6$, $x = 0.7$, $x = 0.8$

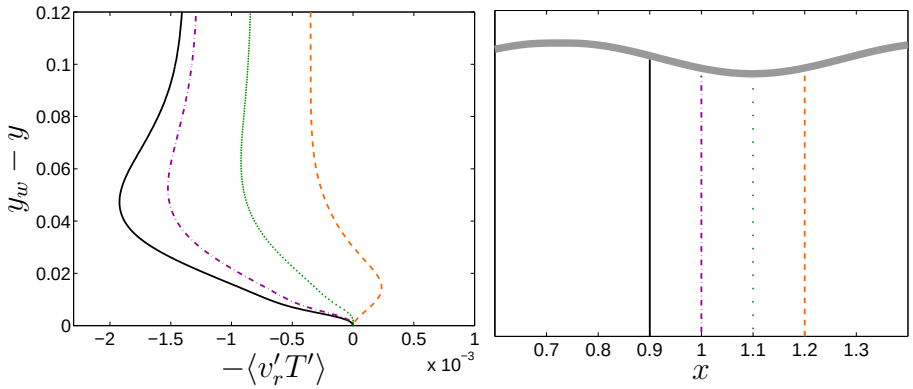

Figure 4.23: Averaged turbulent heat flux component $-\langle v_r' T' \rangle$ outside the recirculation zone at locations $x = 0.9$, $x = 1.0$, $x = 1.1$, $x = 1.2$

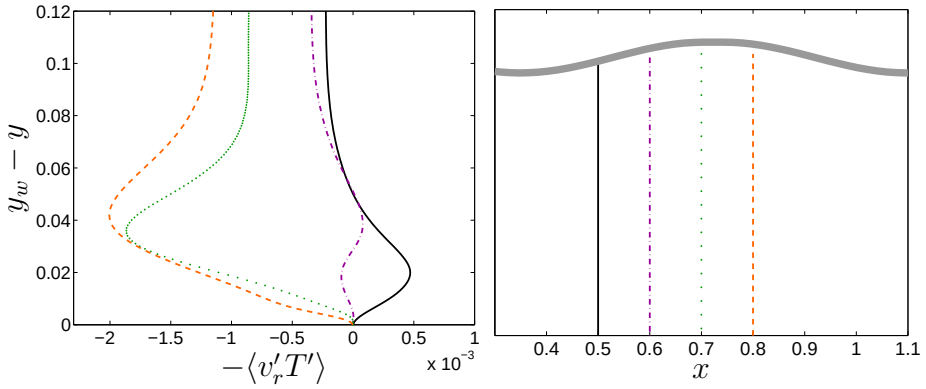

Figure 4.24: Averaged turbulent heat flux component $-\langle v_r' T' \rangle$ inside the recirculation zone at locations $x = 0.5$, $x = 0.6$, $x = 0.7$, $x = 0.8$

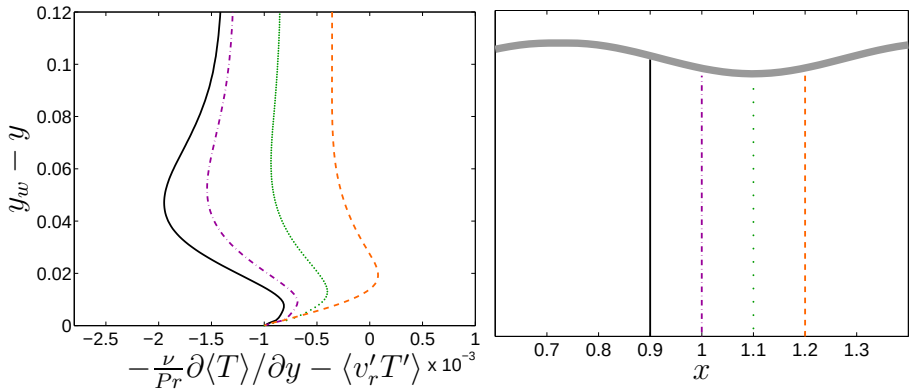

Figure 4.25: Averaged total heat flux component $-\frac{\nu}{Pr}\partial\langle T\rangle/\partial y - \langle v_r' T'\rangle$ outside the recirculation zone at locations $x = 0.9$, $x = 1.0$, $x = 1.1$, $x = 1.2$

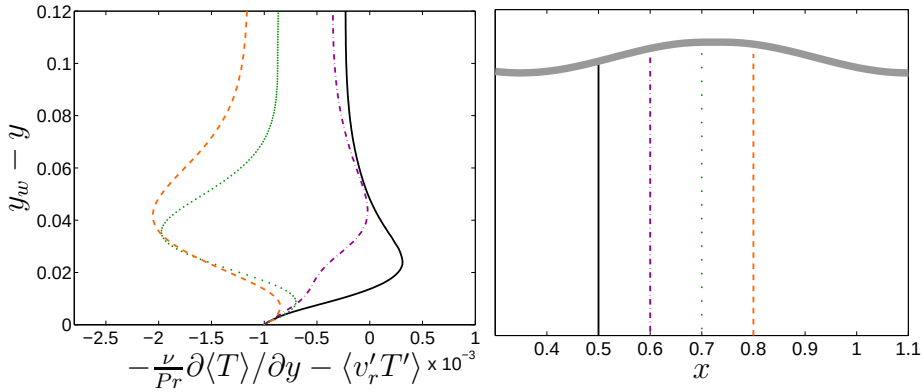

Figure 4.26: Averaged total heat flux component $-\frac{\nu}{Pr}\partial\langle T\rangle/\partial y - \langle v_r' T'\rangle$ inside the recirculation zone at locations $x = 0.5$, $x = 0.6$, $x = 0.7$, $x = 0.8$

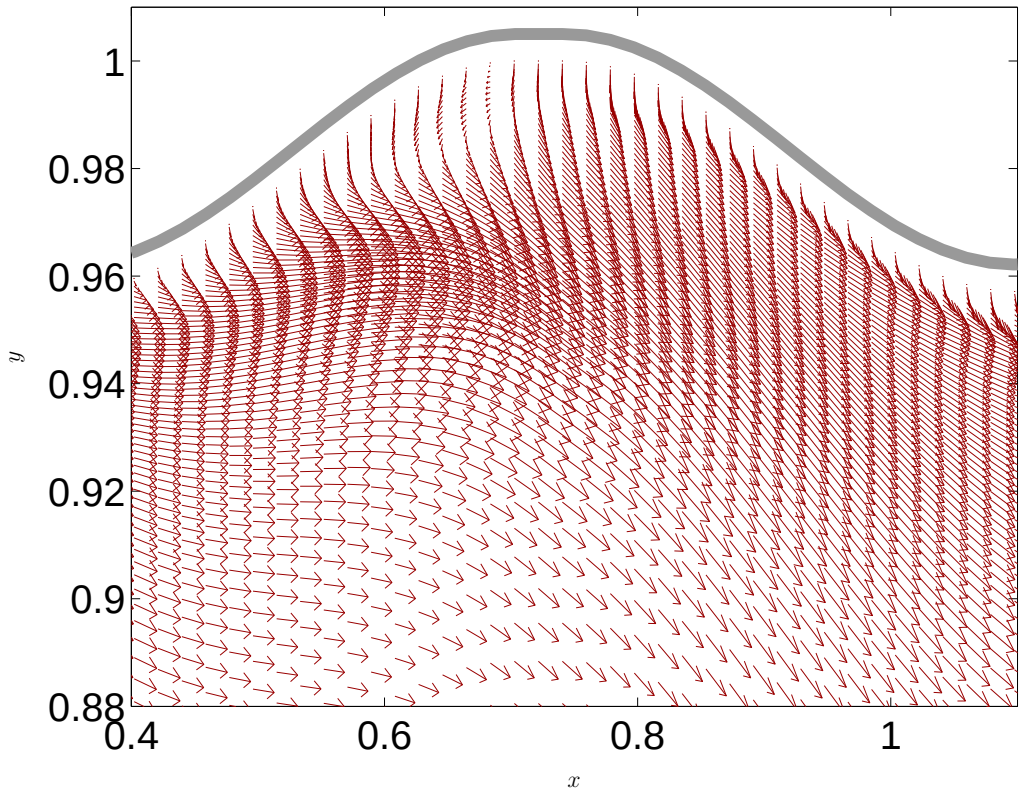

Figure 4.27: Viscous and turbulent heat flux in each computational node

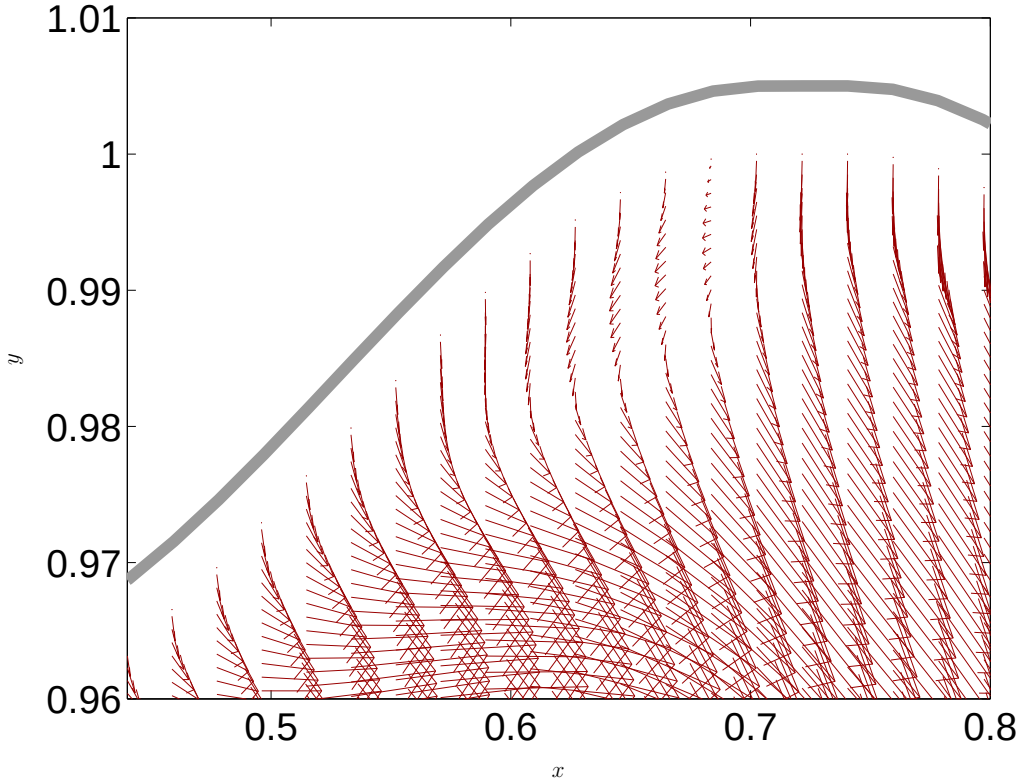

Figure 4.28: Viscous and turbulent heat flux focusing on the recirculation zone

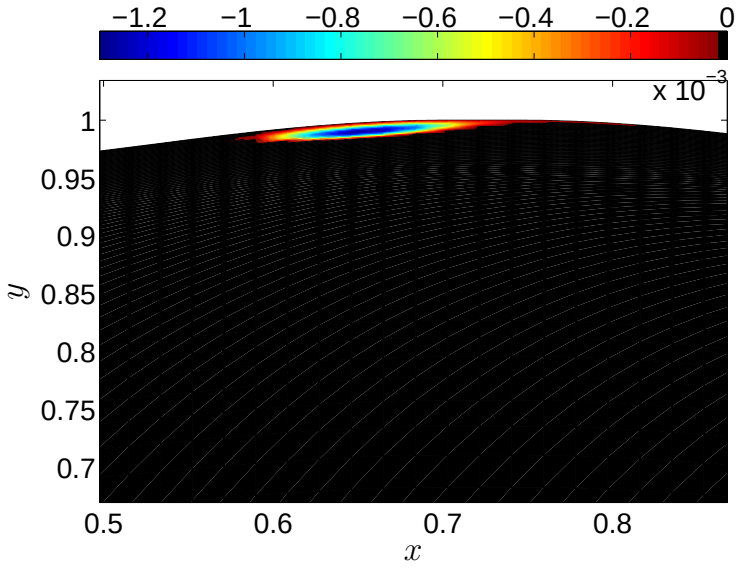

Figure 4.29: Negative values in the x-component of the viscous and turbulent heat flux

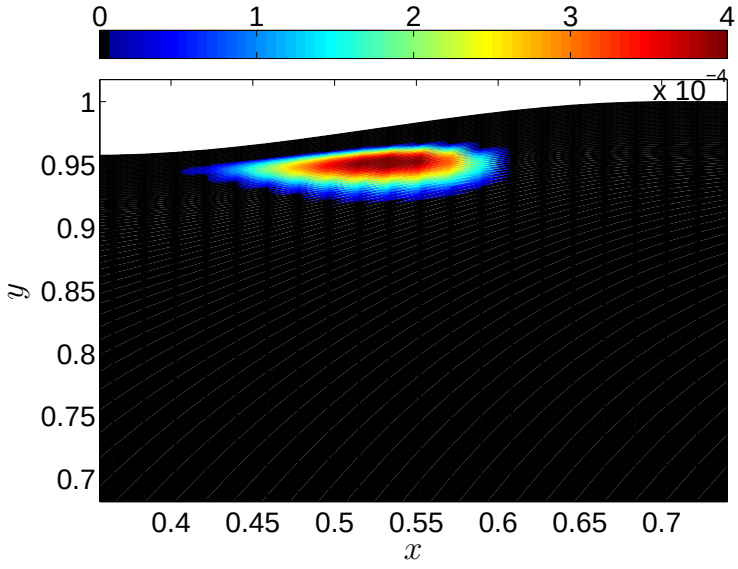

Figure 4.30: Positive values in the y-component of the viscous and turbulent heat flux

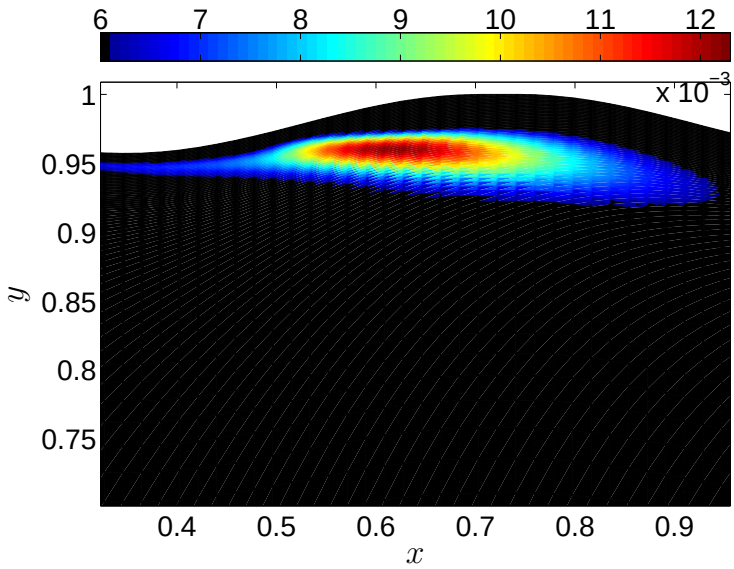

Figure 4.31: Values in the x-component of the viscous and turbulent heat flux greater then 6×10^{-3}

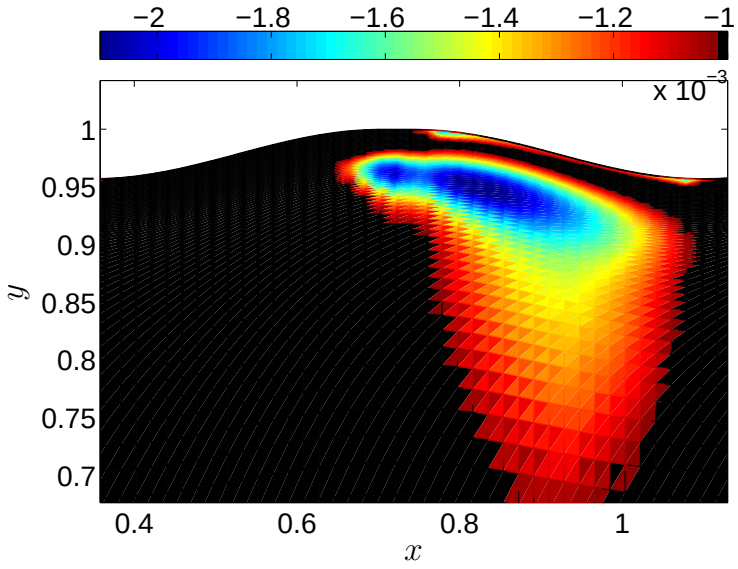

Figure 4.32: Values in the y-component of the viscous and turbulent heat flux less then -10^{-3}

Chapter 5

Summary and conclusion

In the present study a simulation of flow and heat transfer on the inner side of a pipe with a corrugated geometric boundary has been conducted. The simulation has been done on a fluid with a Prandtl number of 3.5,and a density of 1.0 using a Large Eddy Simulation with conditions keeping a mean flow $u_b = 1$, fixing the Reynolds number as $Re_d = 10^4$ for the lengthscale of $R = 1$ corresponding to the radius. A constant heat flux $q = 10^{-3}$ is used at the geometric boundary.

In this simulation the geometry gives rise to a small recirculation zone in at the largest radius of the pipe. In connection to this recirculation the friction coefficient dropps and becomes negative. On the other hand the decreasing radius feature of a corrugation increases the friction coefficient to a value 3.7 times the value of a straight pipe. The dimensionless pressure drop was 2.2 times greater then for a straight pipe.

The average over the resulting Nusselt number was 1.24 times the constant value for a straight pipe. In connection to this recirculation the local Nusselt number drops to values below the ones obtained for a straight pipe with a minimum 0.64 times that for a straight pipe at $x = 0.57$. It is further observed that the periodic wall temperature peaks in the recirculation zone at $x = 0.57$ matching up the Nusselt extremum.

Outside the recirculation zone the local Nusselt number instead increased to a maximum value of 1.8 times the value for a straight pipe, this at $x = 1.0$. In this region, after the reattachment point, an increase in the turbulent intensity is found in connection to the rising Nusselt number.

A more detailed examination of the heat flux shows first that the viscous part is affected a lot less then the turbulent part. It is found that this results in large deviations in the total behaviour of the heat flux vector, related to

the straight pipe case, when the geometry is altered. Especially four different behaviours are observed.

1. The new geometry increases the heat transfer in the radial direction away from the wall in the region of rising slope in the corrugation. This occurs both for the near wall behaviour and some smaller distance away from the wall (figure 4.32). In the same region the Nusselt number is seen to increase.

2. In the recirculation zone the heat flux goes against the stream direction near the wall up until $x = 0.57$ where the maximum in the periodic temperature is observed (figure 4.29).

3. Some small distance from the wall right upstream of $x = 0.57$ the radial component of the heat flux goes towards the wall or is close to zero, blocking heat transfer in the radial direction toward the centerline (figure 4.30).

4. Right below the recirculation zone, there is a large increase of the heat flux in the streamwise direction, meeting up the transport away from the wall.

Comparing with the straight pipe case it is concluded that the turbulent fluctuations are mainly responsible for these changes in the heat transfer. Although the transport locally gets worse than the case of a straight pipe near the temperature peak, this is well compensated in the region where the transport is better than the straight pipe case. It can be hypothised that the better performance is related to the rising feature of the corrugation and the increase in turbulence that is observed in this region and that the local loss in performance is related to the formation of the accumulated increase of the thermal energy. It should though be stressed that there is no definite possiblity to evaluate this hypothesis from the present simulations. The present simulation deals with a symmetric geometry in the two slopes of the corrugation. Future investigations of a non-symmetric setting of the slopes whould be interesting and could shed light on the definite answer to the effect of the corrugation and the importance of the region of accumulated thermal energy.

Appendix

Example of G3DMESH script file

The following script generates a computational mesh for a corrugated domain with a 90 degree azimuthal extension.

```
!#####################################################
!# Script for G3DMESH, corrugated mesh generation  #
!#####################################################
! File name
volsol=$version

!##############
!# Geometry   #
!##############
1.5                 =LENGTH
1.                  =HEIGHT
1.57079             =WIDTH


!#########################
!# Define number of nodes #
!#########################
81      =NI_P
81      =NJ_P
65      =NK_P

!#################################
! First wall node point distance #
!#################################

LENGTH NI_P 1. -   /  =DWALL1
```

```
LENGTH NI_P 1. -   /  =DWALL2
0.1                   =DWALL3
0.001                 =DWALL4
WIDTH NK_P 1. -    /  =DWALL5
WIDTH NK_P 1. -    /  =DWALL6

!####################
! Define stretching #
!####################
1. CHS =H


!##############################
!# Start mesh generation here #
!##############################

!########################################
!# Define the block structure of the grid #
!########################################
DEFMSH
1
NI_P  NJ_P  NK_P


!--------------------------------------
!- First (and only) block created here -
!--------------------------------------

!#####
!# 1 #
!#####
CURV2
1  1 1 1 1 NI_P
1
0.     0. 0. DWALL1
1
LENGTH 0. 0. DWALL2
0.

!##############################
!# 2, corrugation defined here #
```

```
!################################
CURV1
1  1 NJ_P 1 1 NI_P
NI_P
   0.0000000e+00   1.0000000e+00   0.0000000e+00
   1.8750000e-02   9.9970920e-01   0.0000000e+00

[ ...

  ---  Parametrized corrugation coordinates goes here ---

          ... ]

   1.4812500e+00   1.0000000e+00   0.0000000e+00
   1.5000000e+00   1.0000000e+00   0.0000000e+00
1 NI_P DWALL1 DWALL2 0.

!#####
!# 3 #
!#####
CURV2
1  1 1 1 3 NJ_P
2
DWALL3
2
DWALL4
UNKNOWN

!#####
!# 4 #
!#####
CURV2
1  NI_P 1 1 3 NJ_P
2
DWALL3
2
DWALL4
UNKNOWN

!#####
!# 5 #
```

```
!#####
FILLB
1  1 1 1 1 3 NI_P NJ_P

!#####
!# 6 #
!#####
COPYB
1  1 1 1 1 3 NI_P NJ_P
1  1 1 NK_P 1 3 NI_P NJ_P

!#####
!# 7 #
!#####
MOVEB
1  1 1 NK_P 1 3 NI_P NJ_P
0. 0. WIDTH

!#####
!# 8 #
!#####
CURV2
1  1 1 1 5 NK_P
2
DWALL5
2
DWALL6
0.

!#####
!# 9 #
!#####
CURV2
1  1 NJ_P 1 5 NK_P
2
DWALL5
2
DWALL6
0.

!######
```

```
!# 10 #
!######
CURV2
1  NI_P 1 1 5 NK_P
2
DWALL5
2
DWALL6
0.

!######
!# 11 #
!######
CURV2
1  NI_P NJ_P 1 5 NK_P
2
DWALL5
2
DWALL6
0.

!######
!# 12 #
!######
FILLB
1  1 1 1 1 5 NI_P NK_P

!######
!# 13 #
!######
FILLB
1  1 1 1 3 5 NJ_P NK_P

!######
!# 14 #
!######
FILLB
1  1 NJ_P 1 1 5 NI_P NK_P

!######
!# 15 #
```

```
!######
FILLB
1  NI_P 1 1 3 5 NJ_P NK_P

!################################################
!# 16, generate cylinder for nice visualization #
!################################################
CYLCAR
1  1 NI_P 1 NJ_P 1 NK_P
0. 0. WIDTH 90.

!-------------------------
!- First block ends here -
!-------------------------

!######################
!# Check all volumes #
!######################
CHECKV
1   1 NI_P 1 NJ_P  1 NK_P


SAVE
[$version].bin

STOP
```

Bibliography

[1] Frank P. Incropera, David P. Dewitt, Theodire L. Bergman, and Adrienne S. Lavine. *Fundamentals of Heat and Mass Transfer*. Wiley, sixth edition edition, 2007.

[2] S. V. Patankar, C. H. Liu, and E. M. Sparrow. Fully developed flow and heat transfer in ducts having streamwise-periodic variations of cross-sectional area. *Journal of Heat Transfer*, 99:180–186, 1977.

[3] D. J. Tritton. *Physical Fluid Dynamics*. Oxford Scientific Publications, Oxford, second edition edition, 1988.

[4] L. E. Reichl. *A Modern Course in Statistical Physics*. Wiley, New York, second edition edition, 1998.

[5] J. N. Reddy. *An Introduction to Continuum Mechanics*. Cambridge University Press, 2008.

[6] H. K. Versteeg and W. Malalasekera. *An Introduction to Computational Fluid Dynamics - the Finite Volume Method*. Pearson Education Limited, Harlow, second edition edition, 2007.

[7] S. Ghosal and P. Moin. The basic equations for the large eddy simulation of turbulent flows in complex geometry. *Journal of Computational Physics*, 118:24–37, 1995.

[8] Frank M. White. *Fluid Mechanics*. McGraw-Hill, sixth edition edition, 2008.

[9] James W. Demmel. *Applied Numerical Linear Algebra*. Siam, 1997.

[10] F. Nicoud and F. Ducros. Subgrid-scale stress modelling based on the square of the velocity gradient tensor. *Flow, Turbulence and Combustion*, 62:183–200, 1999.

[11] Lars Davidson and Bijan Farhanieh. Calc-bfc , a finite-volume code employing collocated variable arrangement and cartesian velocity components for computation of fluid flow and heat transfer in complex three-dimensional geometries. Technical Report 95/11, Department of Thermo and Fluid Dynamics, Chalmers Univeristy of Technology, Gteborg, nov 1995.

[12] L. Davidson and S. H. Peng. Hybrid les-rans modelling: a one-equation sgs model combined with a $k-\omega$ model for prediciting recirculated flows. *International Journal for Numerical Methods in Fluids*, 43:1003–1018, 2003.